DTIC
ELECTE
JUL 20 1990
S
B
D
Cx

JAI

JAI ASSOCIATES, INC.
SCIENCE & ENGINEERING CONSULTANTS

JAI Associates, Inc. Technical Report 90-01

NUMERICAL SIMULATIONS OF
BLADE-VORTEX INTERACTIONS AND
LIFTING HOVERING ROTOR FLOWS

by

Ganapathi R. Srinivasan

JAI Associates, Inc.

P. O. Box 293

Mountain View, California 94042

April 1990

REPORT DOCUMENTATION PAGE

1a. REPORT SECURITY CLASSIFICATION Unclassified			1b. RESTRICTIVE MARKINGS			
2a. SECURITY CLASSIFICATION AUTHORITY			3. DISTRIBUTION / AVAILABILITY OF REPORT Approved for public release; distribution unlimited.			
2b. DECLASSIFICATION / DOWNGRADING SCHEDULE						
4. PERFORMING ORGANIZATION REPORT NUMBER(S) JAIA TR-90-1			5. MONITORING ORGANIZATION REPORT NUMBER(S) ARO 25575.7-EG			
6a. NAME OF PERFORMING ORGANIZATION JAI Associates, Inc		6b. OFFICE SYMBOL (If applicable)	7a. NAME OF MONITORING ORGANIZATION U. S. Army Research Office			
6c. ADDRESS (City, State, and ZIP Code) P. O. Box 293, Mountain View California 94042			7b. ADDRESS (City, State, and ZIP Code) P. O. Box 12211 Research Triangle Park, NC 27709-2211			
8a. NAME OF FUNDING / SPONSORING ORGANIZATION U. S. Army Research Office		8b. OFFICE SYMBOL (If applicable)	9. PROCUREMENT INSTRUMENT IDENTIFICATION NUMBER DAAL03-88-C-0006			
8c. ADDRESS (City, State, and ZIP Code) P. O. Box 12211 Research Triangle Park, NC 27709-2211			10. SOURCE OF FUNDING NUMBERS			
			PROGRAM ELEMENT NO	PROJECT NO.	TASK NO.	WORK UNIT ACCESSION NO

11. TITLE (Include Security Classification)

NUMERICAL SIMULATIONS OF BLADE-VORTEX INTERACTIONS AND LIFTING HOVERING ROTOR FLOWS

12. PERSONAL AUTHOR(S)   Ganapathi R. Srinivasan

13a. TYPE OF REPORT FINAL	13b. TIME COVERED FROM Feb. 88 TO Feb. 90	14. DATE OF REPORT (Year, Month, Day) April 1990	15. PAGE COUNT 72 pages

16. SUPPLEMENTARY NOTATION   The view, opinions and/or findings contained in this report are those of the author(s) and should not be construed as an official Department of the Army position, policy, or decision, unless so designated by other documentation.

17.	COSATI CODES		18. SUBJECT TERMS (Continue on reverse if necessary and identify by block number)
FIELD	GROUP	SUB-GROUP	Unsteady, viscous, lifting, hover, helicopter rotor,
			Transonic flow, Parallel and Oblique, Blade, Vortex

19 ABSTRACT (Continue on reverse if necessary and identify by block number)

This report presents viscous, three-dimensional numerical solutions of two related problems of a helicopter rotor. An implicit, finite-difference numerical procedure is used for the solution of the thin layer Navier-Stokes equations to simulate the flowfield solutions of 1) helicopter rotor blade encountering a passing concentrated line vortex, and 2) a lifting hovering rotor, at both sub- and super-critical flowfield conditions. For the first problem, the Euler equations were also solved independently to assess the importance of the viscous effects in the interacting flowfield. For this problem, a prescribed vortex

20 DISTRIBUTION / AVAILABILITY OF ABSTRACT ☐ UNCLASSIFIED/UNLIMITED ☐ SAME AS RPT. ☐ DTIC USERS	21. ABSTRACT SECURITY CLASSIFICATION Unclassified	
22a NAME OF RESPONSIBLE INDIVIDUAL	22b. TELEPHONE (Include Area Code)	22c. OFFICE SYMBOL

DD FORM 1473, 84 MAR   83 APR edition may be used until exhausted.   SECURITY CLASSIFICATION OF THIS PAGE
All other editions are obsolete.   UNCLASSIFIED

method is adopted to preserve the structure of the interacting vortex. Both parallel and oblique blade-vortex interactions have been calculated. The sample cases considered for the calculations correspond to the wind tunnel model rotor test conditions. Comparison of the numerical results with the test data show good agreement for both parallel and oblique interactions at subsonic and transonic tip speeds. The viscous effects appear to be not very important for the interactions considered here.

The second problem considered is that of calculating lifting hovering rotor flowfields without using any *ad hoc* wake models. The induced effects of the wake, including the interaction of tip vortices with successive blades, are captured as a part of the overall flowfield solution and hence no wake models are used. In order to preserve the structure of the vortex wake, a completely upwind finite-difference numerical precedure is used for this problem. Comparison of the numerical results show excellent agreement with the experimental data and with the previously published Navier-Stokes calculations that used a simple wake model. These results are the first ever Navier-Stokes calculations presented with the wake capture capability for a lifting hovering rotor.

SUMMARY

This report presents viscous, three-dimensional numerical solutions of two related problems of a helicopter rotor. An implicit, finite-difference numerical procedure is used for the solution of the thin layer Navier-Stokes equations to simulate the flowfield solutions of 1) helicopter rotor blade encountering a passing concentrated line vortex, and 2) a lifting hovering rotor, at both sub- and super-critical flowfield conditions. For the first problem, the Euler equations were also solved independently to assess the importance of the viscous effects in the interacting flowfield. For this problem, a prescribed vortex method is adopted to preserve the structure of the interacting vortex. Both parallel and oblique blade-vortex interactions have been calculated. The sample cases considered for the calculations correspond to the wind tunnel model rotor test conditions. Comparison of the numerical results with the test data show good agreement for both parallel and oblique interactions at subsonic and transonic tip speeds. The viscous effects appear to be not very important for the interactions considered here.

The second problem considered is that of calculating lifting hovering rotor flowfields without using any *ad hoc* wake models. The induced effects of the wake, including the interaction of tip vortices with successive blades, are captured as a part of the overall flowfield solution and hence no wake models are used. In order to preserve the structure of the vortex wake, a completely upwind finite-difference numerical precedure is used for this problem. Comparison of the numerical results show excellent agreement with the experimental data and with the previously published Navier-Stokes calculations that used a simple wake model. These results are the first ever Navier-Stokes calculations presented with the wake capture capability for a lifting hovering rotor.

v

vi

FOREWORD

TABLE OF CONTENTS

x

LIST OF SYMBOLS

a	= speed of sound
a_o	= vortex core radius, see Eq. (6)
a_∞	= free stream sound speed
b	= rotor diameter
C	= characteristic length scale, chord of the blade
C_w	= chord of the vortex generating wing
C_p	= pressure coefficient, based on local dynamic pressure
e	= total energy per unit volume
$\widehat{F}, \widehat{G}, \widehat{H}$	= flux vectors
J	= Jacobian of the coordinate transformation
M_∞	= free stream Mach number, forward speed of the rotor
M_{tip}	= tip Mach number of the rotor blade
p	= static pressure
p_∞	= free stream pressure
Pr	= Prandtl number
$\widehat{Q}$	= flowfield vector of conservative variables
r	= radial distance from the vortex center
r_B	= rotor reference station normalized by R (= 2y/b)
R	= rotor radius
$R(t)$	= rotational matrix, see Eq. (4)
Re	= Reynolds number
$\widehat{S}$	= viscous flux vector
u_∞	= free stream velocity
u, v, w	= velocity components
v_θ	= tangential velocity of the vortex
U, V, W	= contravariant velocity components

x, y, z, t = inertial coordinates

x_o, z_o = vortex offset position relative to the rotor axis

$\tilde{x}_v, \tilde{z}_v$ = distance from blade leading edge to the line vortex

$\tilde{x}, \tilde{y}, \tilde{z}, \tilde{t}$ = blade attached coordinates

α_t = collective pitch angle, degrees

γ = ratio of specific heats

Γ = circulation for the vortex

$\widehat{\Gamma}$ = dimensionless strength of the vortex, $\Gamma/(a_\infty C)$

μ = viscosity coefficient, advance ratio

ξ, η, ζ, τ = generalized curvilinear coordinates

ρ_∞ = free stream density

ρ = density

ψ = azimuthal angle

Ω = angular velocity of the rotor

LIST OF FIGURES

1. INTRODUCTION

The accurate simulation of the flowfield of a helicopter rotor is still one of the most complex and challenging problems of applied aerodynamics. This is true in spite of the availability of the present day supercomputers of Cray-2 class and improved numerical algorithms. The major reason for this is that the flowfield of a rotor in forward flight is highly three-dimensional, unsteady and viscous, with pockets of transonic flow near the blade tips on the advancing blades and regions of dynamic stall on the retreating blades. In addition, the blades also shed complex vortical wakes; the concentrated tip vortices shed by these blades generally pass close to the following blades. The close encounter of these (force free) concentrated vortices with the rotor blades induces unsteady load fluctuations and acoustic noise. Some of the complexities associated with such a flowfield are delineated in a schematic of a helicopter rotor in forward flight in Fig. 1.

The spiralling vortex sheet emanating from each of the blades of the rotor has a profound influence on the performance of the helicopter. It not only alters the effective pitch angle of the blades and thus the airloads, but also produces highly nonlinear interactions of the vortex with the rotor flowfield. It is possible that such interactions might produce vortex induced boundary layer separation which results in a sudden loss of lift and increase in drag. An accurate simulation of the rotor flowfield, therefore, must consider the induced effects of the vortex wake including the effects of blade-vortex interactions (BVI).

Numerical simulations of the vortex wakes are being attempted only recently after bigger and faster computers have become available (Ref. 1). These investigations have had some limited success to date in simulating the formation and initial roll up processes. On the other hand, much of the progress in modeling the blade-vortex interaction has been hampered by the lack of development of theoretical and/or numerical techniques

1

to preserve the structure of the concentrated vortices, when convecting in the flowfield, without significant diffusion. The study of blade-vortex interaction has been the subject of numerous recent research papers (Refs. 2-10). These studies have considered different methods of preserving the concentrated vortex in the flowfield. Among these, the vortex-fitting technique (also called the split potential formulation in potential flow methods) has been demonstrated to be a very effective method in preserving the vortex even when the computational grid is sparse. This method has also proven very economical (Ref. 5) compared to a more exact formulation used in Ref. 3.

Accurate simulations of the flowfield of a helicopter rotor in hover or in forward flight require an accurate description of the vortex structure and its position in the wake. The Navier-Stokes methods are the only methods that can provide this information. To compute such an information on a routine basis for a design analysis is perhaps prohibitively expensive even with the present day supercomputers. This is the reason that simple methods, based on linear aerodynamics, have been developed for use in industry (see for example Refs. 11-12).

To date, many advances have been made to calculate these complex flowfields by the use of simpler equations of fluid motion, such as full potential, coupled with empirical wake models to bring-in the influence of the vortex wake (Ref. 8). Such methods have been specialized for each blade shape and planform and therefore are not very general. Nevertheless, these methods have been useful to the industry and are being used in the design analysis on a routine basis. There is no doubt that the weak link in the above methodology is the wake modeling as these methods cannot handle arbitrary configurations and high supercritical flow conditions. Alternative to the prescribed wake models used in the above methods, the present study will present a numerical method to capture the wake and its influence as a part of the overall flowfield solution. This means that the present method does not use any *ad hoc* wake models.

It should be pointed out that the concept of wake capture is not new and has, in

fact, been utilized by several researchers to investigate the hovering rotor problem. In particular, the works of Refs. 13-17 are to be mentioned for the Euler and flow potential methods. These studies have shown promise with limited success. The main ingredient that is responsible for the formation of tip vortices, namely the viscosity, is absent in these methods. While the role of viscosity is clear, its importance in these flows is uncertain at this stage. This will be investigated in the present study.

The purpose of this study, therefore, is to devise numerical methods for the solution of the Navier-Stokes equations to accurately calculate the flowfield of a helicopter rotor, including the effects of blade-vortex interactions. In particular, this report will attempt to demonstrate the ability of the current Navier-Stokes methods to 1) calculate the unsteady, three-dimensional, blade-vortex interaction (BVI) flowfield, for both parallel and oblique blade-vortex interactions for a model helicopter rotor problem (see for example Refs. 18-19), and 2) calculate the flowfield of a lifting hovering rotor by capturing the wake and its influence as a part of overall solution method corresponding to the experimental conditions of a model rotor test (Ref. 20).

2. GOVERNING EQUATIONS AND NUMERICAL SCHEME

The governing partial differential equations are the unsteady, thin layer Navier-Stokes equations. In this study, the thin layer Navier-Stokes code recently written specifically for helicopter rotor applications (Ref. 21) will provide the starting point for further modifications to calculate the blade-vortex interaction flowfield first and later the lifting hovering rotor flowfield. In order to assess the importance of viscous effects in the blade-vortex interacting flowfields, both the Euler and the thin layer Navier-Stokes equations have been solved. (The Euler calculations are performed by turning off the viscous terms in the Navier-Stokes equations set and appropriately modifying the surface boundary condition.) The mathematical formulation presented in the following paragraphs is for the solution of thin layer Navier-stokes equations with the added feature of introducing a prescribed vortex.

For generality, the equations are transformed from the inertial Cartesian reference frame (x, y, z, t) to the arbitrary curvilinear coordinate frame (ξ, η, ζ, τ) that moves with the blade, while retaining strong conservation law-form to capture shock waves. The transformed equations, following Ref. 22, can be written as

$$\partial_\tau(\widehat{Q} - \widehat{Q}_\circ) + \partial_\xi(\widehat{F} - \widehat{F}_\circ) + \partial_\eta(\widehat{G} - \widehat{G}_\circ) + \partial_\zeta(\widehat{H} - \widehat{H}_\circ) = \epsilon Re^{-1}\partial_\zeta \widehat{S} \qquad (1)$$

where

4

$$\widehat{Q} = J^{-1} \begin{bmatrix} \rho \\ \rho u \\ \rho v \\ \rho w \\ e \end{bmatrix}, \ \widehat{F} = J^{-1} \begin{bmatrix} \rho U \\ \rho u U + \xi_x p \\ \rho v U + \xi_y p \\ \rho w U + \xi_z p \\ U(e+p) - \xi_t p \end{bmatrix},$$

$$\widehat{G} = J^{-1} \begin{bmatrix} \rho V \\ \rho u V + \eta_x p \\ \rho v V + \eta_y p \\ \rho w V + \eta_z p \\ V(e+p) - \eta_t p \end{bmatrix}, \ \widehat{H} = J^{-1} \begin{bmatrix} \rho W \\ \rho u W + \zeta_x p \\ \rho v W + \zeta_y p \\ \rho w W + \zeta_z p \\ W(e+p) - \zeta_t p \end{bmatrix} \tag{2}$$

and $\epsilon = 0$ for Euler equations, and $\epsilon = 1$ for thin-layer Navier-Stokes equations. Here $\widehat{Q}$ is the unknown flowfield vector and $\widehat{Q}_o$ is the solution of the Euler equations for a prescribed line vortex aligned with the uniform free stream of Mach number, M_∞, in the y-direction (see Fig. 2). The terms $\widehat{F}$, $\widehat{G}$, $\widehat{H}$ and $\widehat{F}_o$, $\widehat{G}_o$, $\widehat{H}_o$ represent the appropriate flux vectors for the two flows, respectively. The hat, represented by ($\widehat{}$), in Eq. (1) denotes quantities scaled by the Jacobian J, e.g., $\widehat{Q} = J^{-1}Q$ etc. The contravariant velocity components U, V and W are defined as

$$U = \xi_t + \xi_x u + \xi_y v + \xi_z w$$

$$V = \eta_t + \eta_x u + \eta_y v + \eta_z w$$

$$W = \zeta_t + \zeta_x u + \zeta_y v + \zeta_z w$$

In the present formulation, ξ lies in the chordwise or wraparound direction, η is in the spanwise direction, and ζ is normal to the blade surface.

The viscous flux vector $\widehat{S}$ is used in the limit of the thin-layer approximation and is given by

$$\widehat{S} = J^{-1} \begin{bmatrix} 0 \\ K_1 u_\zeta + K_2 \zeta_x \\ K_1 v_\zeta + K_2 \zeta_y \\ K_1 w_\zeta + K_2 \zeta_z \\ K_1(Pr^{-1}(\gamma - 1)^{-1}(a^2)_\zeta + ((q^2)/2)_\zeta) \\ + K_2 K_3 \end{bmatrix} \tag{3}$$

5

where

$$K_1 = \mu(\zeta_x^2 + \zeta_y^2 + \zeta_z^2)$$

$$K_2 = \mu(\zeta_x u_\zeta + \zeta_y v_\zeta + \zeta_z w_\zeta)/3$$

$$K_3 = \zeta_x u + \zeta_y v + \zeta_z w$$

$$q^2 = u^2 + v^2 + w^2$$

(4)

In this equation, a is the speed of sound, κ is the coefficient of thermal conductivity and μ is the viscosity coefficient computed as the sum of laminar and turbulent contributions. Sutherland's equation is used for laminar viscosity and the two-layer algebraic eddy viscosity model of Baldwin and Lomax (Ref. 23) is used to calculate the turbulent eddy viscosity, after minor modifications to account for the moving blade surface. Also, J is the transformation Jacobian, whose inverse is written as

$$J^{-1} = x_\xi y_\eta z_\zeta + x_\zeta y_\xi z_\eta + x_\eta y_\zeta z_\xi - x_\xi y_\zeta z_\eta - x_\eta y_\xi z_\zeta - x_\zeta y_\eta z_\xi$$

The velocity components u, v, w and the pressure, p, are related to the total energy per unit volume, e, through the equation of state for a perfect gas by

$$p = (\gamma - 1)(e - \frac{\rho}{2}(u^2 + v^2 + w^2))$$

(5)

The primitive variables of Eq. (1), viz., the density ρ, the mass fluxes $\rho u, \rho v, \rho w$ and the energy per unit volume e, are normalized by the free stream reference quantities and the pressure p by γp_∞. The reference length and velocity scales are the chord of the blade, C, and free stream speed of sound, a_∞, respectively. The details of the metrics of transformation $(\xi_t, \xi_x, \xi_y, \xi_z)$, $(\eta_t, \eta_x, \eta_y, \eta_z)$ and $(\zeta_t, \zeta_x, \zeta_y, \zeta_z)$ can be found in Ref. 22.

In the above equations $u, v,$ and w are the Cartesian components of velocity in the inertial coordinate system (x, y, z, t). In the present formulation Eq. (1) is solved

6

in the inertial frame of reference with the boundary conditions applied on the rotating blade. The inertial coordinates $\mathbf{X} = (x, y, z, t)$ are related to the blade-fixed coordinates $\mathbf{X_b} = (\tilde{x}, \tilde{y}, \tilde{z})$ through the relation given by

$$X(x, y, z) = R(t)X_b(\tilde{x}, \tilde{y}, \tilde{z})$$
$$t = \tilde{t}$$

(6)

where $R(t)$ is the rotational matrix (Ref. 24) given by

$$R(t) = \begin{bmatrix} \cos\Omega\tilde{t} & -\sin\Omega\tilde{t} & 0 \\ \sin\Omega\tilde{t} & \cos\Omega\tilde{t} & 0 \\ 0 & 0 & 1 \end{bmatrix}$$

(7)

Here Ω is the angular velocity of the rotor and Ωt represents the azimuth sweep of the rotor blade.

The equations set, Eq. (1), is solved using a two-factor, implicit, finite-difference numerical scheme (Ref. 25), that uses spatial central-differencing in the η and ζ directions and upwind-differencing in the ξ direction and is given by

$$\begin{aligned}
&\left[I + h\delta_\xi^b(\widehat{A}^+)^n + h\delta_\zeta\widehat{C}^n - hRe^{-1}\bar{\delta}_\zeta J^{-1}\widehat{M}^n J - D_i|_\zeta\right] \\
&\times \left[I + h\delta_\xi^f(\widehat{A}^-)^n + h\delta_\eta\widehat{B}^n - D_i|_\eta\right](\Delta\widehat{Q}^n - \Delta\widehat{Q}_\circ^n) = \\
&-\Delta t\{\delta_\xi^b[(\widehat{F}^+)^n - (\widehat{F}_\circ^+)^n] + \delta_\xi^f[(\widehat{F}^-)^n - (\widehat{F}_\circ^-)^n] \\
&+ \delta_\eta(\widehat{G}^n - \widehat{G}_\circ^n) + \delta_\zeta(\widehat{H}^n - \widehat{H}_\circ^n) - Re^{-1}\bar{\delta}_\zeta(\widehat{S}_\zeta^n)\} \\
&- (D_e|_\eta + D_e|_\zeta)(\widehat{Q}^n - \widehat{Q}_\circ^n)
\end{aligned}$$

(8)

where $h = \Delta t$ for first-order time accuracy. Here δ is typically a three-point, second-order-accurate, central difference operator, $\bar{\delta}$ is a midpoint operator used with the viscous terms, and the operators δ_ξ^b and δ_ξ^f are backward and forward three-point difference operators. The time index is denoted by n such that $t = (n\Delta t)$, and $\Delta\widehat{Q}^n = \widehat{Q}^{n+1} - \widehat{Q}^n$. The flux vector $\widehat{F}$ has been split into $\widehat{F}^+$ and $\widehat{F}^-$, according to its eigenvalues (Ref. 26)

7

and the matrices $\widehat{A}^{\pm}$, $\widehat{B}$, $\widehat{C}$, and $\widehat{M}$ result from the local linearization of fluxes about the previous time level (see Ref. 22). The finite-difference scheme described in Eq. (5) uses flux-splitting in ξ direction and central differencing in the η and ζ directions. As a consequence, numerical disspation terms denoted by D_i and D_e are employed in the η and ζ directions, and are given as combinations of second- and fourth-differences as follows (Ref. 27).

$$D_e|_\eta = (\Delta t)J^{-1}(|\eta|_x + |\eta|_y + |\eta|_z)\left[\epsilon_2 \bar{\delta} \frac{|\bar{\delta}^2 p|}{|(1 + \bar{\delta}^2)p|}\bar{\delta} + \epsilon_4 \bar{\delta}^4\right]|_\eta J$$

$$D_i|_\eta = (\Delta t)J^{-1}(|\eta|_x + |\eta|_y + |\eta|_z)\left[\epsilon_2 \bar{\delta} \frac{|\bar{\delta}^2 p|}{|(1 + \bar{\delta}^2)p|}\bar{\delta} + 3\epsilon_4 \bar{\delta}^4\right] J \qquad (9)$$

In the vicinity of shock waves, the fourth-difference terms can cause oscillations, so it is desirable to drop these terms and rely only on the second-difference terms. In the above expression, p is the nondimensionalized fluid pressure and ϵ_2 is $O(1)$ while ϵ_4 is $O(0.1)$. In transonic flow the term $(|\eta|_x + |\eta|_y + |\eta|_z)$ is an estimate to the spectral radius of the matrix B for variables that have been nondimensionalized with respect to the sound speed. since $(|\eta|_x + |\eta|_y + |\eta|_z)$ does not contain any fluid variable, it can be left as the coefficient to the dissipation operator without affecting the weak conservation form of the difference equations. The implicit second difference numerical dissipation operators were chosen to keep the left hand side factors block tridiagonal, and as D_i works on δQ, accuracy is not impaired.

The factored operators in Eq. (8) are solved by sweeping in the ξ direction and inverting tridiagonal matrices with 5 x 5 blocks for the other two directions. Currently, a significant part of the computational time is taken to form the plus and minus Jacobian matrices for the flux vector $\widehat{F}$ with this numerical scheme. However, this effort has been reduced by computing $\widehat{A}^+$ and $\widehat{A}^-$ at every other point (in both η and ζ directions) and averaging to obtain the matrices at the intermediate points. The numerical code is

8

vectorized for the Cray-2 supercomputer.

In writing Eq. (5) it is assumed that $\widehat{A}_o^{\pm} \approx \widehat{A}^{\pm}$, $\widehat{B}_o \approx \widehat{B}$, and $\widehat{C}_o \approx \widehat{C}$ where the Jacobian matrices $\widehat{A}_o^{\pm}$, $\widehat{B}_o$ and $\widehat{C}_o$ correspond to the prescribed-vortex flowfield. In the absence of vortex interaction, the prescribed-disturbance flowfield reduces to a free stream.

In using this numerical algorithm for the physical problem of blade-vortex interaction presented here, a note of caution is in order. As noted before, the numerical scheme is second-order accurate in space. Although it is desirable to have higher-order accuracy in space, it turns out that the present algorithm is numerically more stable if this accuracy is decreased slightly from second-order. Also, in evaluating the right hand side of Eq. (5), it is desirable to calculate the derivatives of individual fluxes first and then taking a difference. This is particularly true for the fluxes in the ζ direction.

The above numerical algorithm is used for the problem of blade-vortex interaction. For calculating the lifting hovering flowfields, a slightly different numerical algorithm is used. The fundamental difference is the use of upwinding in all three directions. This feature coupled with a simplified left-hand-side has produced an efficient and accurate numerical scheme that is about five times computationally efficient. These additional features are utilized from the works of Ref. 28. The use of Roe's upwinding eliminates the addition of explicit numerical dissipation to control the stability of the code and thus is known to produce less dissipative solutions. This feature, coupled with a fine grid description in the tip region would enable better description of the wake simulation. It is hoped that the preservation of the wake structure in the flowfield, at least in the initial formation and roll-up stages, would be better in the absence of additional numerical viscosity.

Body-conforming finite-difference grids have been used in the present study.

9

The helicopter rotor blades considered are of rectangular plan form with no twist or taper. The grid topologies consist of warped spherical O-O for the first problem and C-H cylindrical grid for the second problem. For the first problem, the flowfield grid is generated using the three-dimensional hyperbolic grid solver of Steger and Chaussee (Ref. 29) with proper clustering in the leading and trailing edge regions and in the tip region. The grid is nearly orthogonal at the surface and the spacing in the normal direction at the surface is chosen to be 0.0002C for the viscous grid and 0.02C for the Euler grid. The viscous computations are done on a grid consisting of 21 points along the span, 101 in the periodic direction around the blade and 31 in the normal direction. The Euler grid is more coarser with only 21x101x15 grid points. The outer grid boundary was chosen to be at 8 chords in all directions for both viscous and inviscid grids.

The C-H cylindrical grid used for the lifting hover calculation appears to be the desirable topology because of the cylindrical nature of the flow. The grid is clustered as before to enable better resolution of the flow. The grid used has approximately one million points with 217 in the chordwise direction, 71 in the spanwise direction and 61 in the normal direction. The spacing near the wall is 0.00005. The smallest spacing at the bevel tip in the spanwise direction is of the order of the semi-thickness of the blade. To test the code a smaller grid was constructed by selecting every other point in all the three directions.

The boundary conditions, both surface and farfield, are applied explicitly. At the rotating blade surface because of the noslip condition for viscous flows, the contravariant velocities U, V and W are set to zero. However, the surface velocity in the inertial frame is nonzero since it is equal to the surface grid velocity, determined by the time metrics ξ_t, η_t and ζ_t as the blade (and the grid attached to it) moves in azimuth. The Euler calculations use an extrapolation of contravariant velocities to the surface. The density at the wall is determined by zeroth-order extrapolation. The pressure along the body

10

surface is calculated from the normal momentum relation (see, for example Ref. 22). Having calculated the density and pressure, the total energy is determined from the equation of state.

At the farfield boundary the flow quantities are either fixed or extrapolated from the interior depending on whether the flow is subsonic or supersonic and if it is of inflow- or outflow-type at the boundary. The characteristic velocities of the Euler equations determine the number of flow properties to be specified to control the reflections of waves from the boundaries. For the subsonic-inflow boundary, four quantities must be specified and one quantity is determined. The four specified here are a Riemann invariant, the entropy, and two tangential velocities; the quantity that is calculated is also a Riemann invariant. For the supersonic-inflow, all flow quantities are specified. At the subsonic-outflow boundaries, only one quantity is specified. For the supersonic-outflow condition all flow quantities are extrapolated from the interior. The plane containing the blade root is chosen very close to the rotation axis of the blade (at $R = 1.0C$) and is also treated as a farfield boundary.

For the hovering rotor problem, the farfield boundary is updated explicitly by means of characteristic-type boundary conditions procedure (Ref. 30), although the effect of using this procedure was found to be unimportant. This is because the Roe's upwinding procedure used in the numerical scheme would otherwise treat the boundaries in a 1-D characteristic sense. At the inboard plane, near the center of rotation, a linear extrapolation is used for density and the three-velocities, and the energy is calculated from the equation of state by prescribing the pressure. A periodicity condition is used to swap the information at the front and back boundaries of the cylidrical grid topology (for a two bladed rotor) for wake capture feature. At the bottom boundary of the cylindrical grid, a boundary condition similar to that prescribed at the farfield boundary in the first problem is imposed explicitly.

11

The interacting line vortex generated upstream of the rotor by a rectangular wing is fixed in the inertial space along a line of constant x. It is assumed to have an analytical representation for the cylindrical velocity distribution given by

$$v_\theta = \frac{C_k \widehat{\Gamma}}{2\pi r} \left(\frac{r^2}{r^2 + a_o{}^2} \right) \tag{10}$$

The constant C_k in the above expression has been determined to be equal to 0.8 by matching the peak tangential velocity with the experimentally measured value at the measured radial distance reported in Ref. 6. The constant a_o is approximately equal to the radius of the viscous core of the vortex (equal to 0.167C in the present case). The induced velocity due to this line vortex is calculated using the Biot-Savart Law and the pressure field is calculated by solving the radial momentum equation; the vortex is initialized well upstream of the interaction region as described in Ref. 5.

3. RESULTS AND DISCUSSION

All the calculations performed in the first part of this study are done in a time-accurate fashion. The test cases calculated correspond to the two sets of experiments of Caradonna et al. (Refs. 18-19) for parallel and oblique blade-vortex interactions. Since one of the purposes of the experiments was to collect data to validate numerical methods, the experimental apparatus was kept simple to ease the representation by numerical methods. The rotor geometry consisted of a two-bladed rigid rotor of approximately 14-chord diameter. The blades have a rectangular planform and consist of an NACA 0012 airfoil with no twist or taper. The rotor blades are essentially nonlifting in the absence of the vortex interaction. The interacting vortex was generated upstream of this rotor by a lifting rectangular wing with an NACA 0015 airfoil. Parallel and oblique BVI are generated by positioning the line vortex along the y-axis ($x_o = 0.0$) and ahead of the y-axis ($x_o < 0.0$) so that the rotor blade encounters the vortex on the advancing side in the first- and second-quadrants of the azimuthal travel as shown in Fig. 2.

As mentioned before, the Navier-Stokes hover code described in Ref. 21 provides the starting point for the present investigation. In this study, this code has been validated against the experimental data of Caradonna and Tung (Ref. 20) for the nonlifting and lifting hover conditions for both the subcritical and the supercritical tip speeds. Although the main focus of the present investigation is to calculate both parallel and oblique blade-vortex interactions, it is necessary to first calculate the base-line rotor-alone flowfield solutions (in the absence of vortex interaction) at the same free stream conditions. Two sets of results for parallel blade-vortex interactions, corresponding to $M_{tip} = 0.6$ and 0.8 and $\mu = 0.2$ and one set of results for oblique blade-vortex interaction corresponding to $M_{tip} = 0.763$ and $\mu = 0.197$, will be presented in the following sections and compared with experimental data. At the Reynolds numbers corresponding to the blade tip speeds in these experiments, the boundary layer on the entire rotor blade could be assumed to

13

be turbulent and, as mentioned before, an algebraic eddy viscosity model of Baldwin and Lomax (Ref. 23) is used for calculating the turbulent viscosity.

3.1 Rotor-Alone Case

The calculation of the rotor-alone flowfield solutions serves two purposes. First, it enables an understanding of the importance of unsteady time-lag effects in shock wave growth and decay as well as the three-dimensionality of the flowfield of the advancing rotor, particularly when the flow is supercritical. Second, it provides the baseline solution to eventually calculate the vortex interaction flowfield.

Figure 3 shows the instantaneous surface pressure distributions for various azimuthal positions of the rotor for the case of $M_{tip} = 0.6$ and $\mu = 0.2$. Examination of the results suggests that at this reference station of $r_B = 0.893$ and for the subcritical flow condition, the flow behaves as if it is quasi-steady and quasi-two-dimensional. In spite of the gradual increase of the blade-element relative speed in the first quadrant and gradual decrease of the same in the second quadrant, the flowfield appears to remain nearly the same at all azimuth locations (as seen in Fig. 3b) indicating that the unsteady time-lag effects are virtually absent for this flow condition and the flow behaves as if it is quasi-steady. In fact, also shown in Fig. 3b is the quasi-steady solution for one azimuth location of $\psi = 90.°$ which is in perfect agreement with the unsteady solutions at different azimuthal positions. Also, the comparison of three-dimensional results of Fig. 3b with the two-dimensional results (Ref. 6) of Fig. 3a shows that these results are nearly identical suggesting that the flow also behaves as if it is quasi-two-dimensional.

At the supercritical tip flow conditions, corresponding to $M_{tip} = 0.8$ and $\mu = 0.2$, the basic rotor flowfield is dominated by the presence of a strong shock wave on the advancing blade over large parts of the first- and second-quadrants. For this advancing rotor, the Euler and Navier-Stokes results of instantaneous surface pressures are shown

14

in Fig. 4 at the radial station $r_B = 0.893$ for different azimuthal positions of the blade. The Euler results show good agreement with the experiments and the Navier-Stokes results have only a qualitative agreement because of the coarse grid. It appears that the shock wave position is under predicted for the Navier-Stokes method and slightly over predicted for the Euler method. For this coarse grid solution, the Navier-Stokes method predicts the decay of the shock much faster in the second-quadrant. On the other hand, the Euler method predicts that the shock wave persists at the $\psi = 180°$ azimuth. Previous two-dimensional Navier-Stokes calculations of the same flow (Ref. 6) had shown strong three-dimensionality and unsteady time-lags in shock wave growth and decay. The two-dimensional assumption for this flow essentially over-predicted the shock wave position and strength, unlike the subcritical flow condition. In contrast, the three-dimensional Euler results seem to follow the experimental observation correctly.

Thus at this flow condition, the flowfield is highly three-dimensional exhibiting strong unsteady time-lag behaviour in the shock wave formation and eventual demise. The unsteady time-lag feature of the flowfield is demonstrated in the surface pressure distributions of Fig. 4 shown for $\psi = 60°$ and $\psi = 120°$ azimuthal positions, which shows that the two results are very different from each other.

In principle, the shock wave should attain its maximum strength when the relative flow speed reaches a maximum value for $\psi = 90°$ blade azimuthal position. However, the shock wave keeps growing in strength even after the blade has passed the $\psi = 90°$ azimuthal position and a weak shock wave seems to persist even at the $\psi = 180°$ azimuth. The strengthening of the shock wave in the first-quadrant and beyond, and the slow demise of it in the second-quadrant, suggests the existence of a strong unsteady time-lag effect at this flow condition. Such a behavior was totally absent at the subcritical flow condition. The presence of the shock wave seems to introduce not only the time-lag in the adjustment of the flow as the blade sweeps in azimuth, but also makes the flow

15

highly three-dimensional.

In contrast to the flow on the advancing side of the rotor blade, the flowfield of the retreating side appears really benign for this nonlifting rotor. The lingering effects of the shock wave, persisting at $\psi = 180,°$ soon die out as the blade sweeps into the third-quadrant. Shown in Fig. 5 are the surface pressure distributions for several azimuthal locations of the blade in third- and fourth-quadrants on the retreating cycle. Since the flowfield is basically subcritical on the retreating side, the plots of Fig. 5 appear to have the same behavior as those of Fig. 3.

Figure 6 shows the surface pressure distributions on the advancing rotor at $r_B = 0.946$ for the flow conditions of $M_{tip} = 0.763$ and $\mu = 0.197$. Since this flow condition is similar to that of the case of Fig. 4, it has the same qualitative behaviour of the flow on the advancing side. As seen in these plots, the Euler calculations are in good agreement with the experimental data.[3] As before, the Navier-Stokes results have only a qualitative agreement for the reasons mentioned before. It is important to mention that the rotor-alone case involves a nonlifting symmetrical blade, for which the pressure distributions should be identical on the upper and lower surfaces. However, the data in Fig. 6, from Ref. 19, seem to have more scatter than the corresponding experimental results from Ref. 18.

3.2 Quasi-steady vs Unsteady Results

Although the flowfield of a lifting helicopter rotor is, in general, unsteady and three-dimensional, a close inspection of the subsonic surface pressure results presented in Fig. 3b suggests that the unsteady and quasi-steady results are nearly the same for this nonlifting flow condition. In fact, a quasi-steady flow calculated by freezing the rotor blade at certain azimuthal locations (say, $\psi = 0.0°$) produces nearly the same flowfield as an unsteady flowfield irrespective of the flow conditions. In the present approach,

16

the unsteady calculations are started from a baseline quasi-steady solution. At the subcritical flow conditions, similar to that presented in Fig. 3, an unsteady calculation can be started from any azimuthal location of the blade because of the quasi-steady and the unsteady solutions being nearly identical at all azimuthal locations. However, this is not true for supercritical flow conditions where shock waves are present in the flowfield. For example, Fig. 7 shows the quasi-steady and unsteady surface pressure distributions for the case of $M_{tip} = 0.8$ and $\mu = 0.2$ at azimuthal locations of $\psi = 60°$ and $120°$. For this flow condition, these results indicate that the quasi-steady assumption over predicts the shock strength at $\psi = 60°$ and under predicts at $\psi = 120°$. Nevertheless, at $\psi = 0.0°$ position, the quasi-steady and unsteady results are nearly identical even for this flow condition. So, for flow conditions that are severe, it is still reasonable to start the unsteady marching from the quasi-steady solution calculated at $\psi = 0.0°$ azimuthal location.

3.3 Parallel Blade-Vortex Interaction

During the unsteady three-dimensional close encounter of a curved tip vortex with a rotating blade, the helicopter rotor undergoes a variety of blade-vortex inter-actions depending on the interaction angle between the leading edge of the rotating blade and the curved line vortex. These interactions are generally unsteady and three-dimensional. One limiting case of such an encounter, for zero interaction angle, is termed parallel interaction (see, for example, Ref. 5). In the experimental configuration consid-ered here, this interaction occurs around $\psi = 180°$ azimuthal position. For an observer riding with the blade (at a given reference station along the span), it appears as though the observer is passing a fixed vortex in the flow. For this reason, this interaction is sometimes approximated as two-dimensional and unsteady.

To calculate accurately the blade-vortex interaction flowfield, it is necessary to preserve the vortex structure without numerical diffusion. As mentioned before, one

17

method that has been demonstrated to work effectively and economically in achieving this is the prescribed-disturbance scheme (Ref. 5). The effectiveness of this scheme is illustrated in Fig. 8 (reproduced from Ref. 7) showing the variation of lift coefficient as a function of the vortex location during an airfoil-vortex interaction. Also shown in this figure is the Euler lift distribution calculated using a conventional (vortex capturing) technique (Ref. 31). Although the two Euler solutions are computed on the same grid, the numerical dissipation associated with the finite grid-spacing progressively weakens the gradients and reduces the effective vortex strength in the conventional method. Also, this numerical error is grid-dependent (the finer the grid the lesser the error); however, it is completely absent in the prescribed-vortex solutions, which are essentially independent of the grid. Hence, the prescribed-disturbance method has been used here for preserving the vortex structure.

3.3.1 Subcritical Interaction

The results of a subcritical parallel BVI are discussed here. This case corresponds to the flow conditions of $M_{tip} = 0.6$, $\mu = 0.2$, and $C_k\widehat{\Gamma} = 0.133$ at a blade reference station (marked AA in Fig.2) $r_B = 0.893$. The interacting vortex is located at $x_o = 0.0$ and $z_o = -0.4$ along the y-axis. To calculate the BVI flowfield, the interacting vortex is initialized with the baseline rotor solution at the azimuthal position of $\psi = 120.°$ The unsteady flow field is monitored as the blade continues to advance in azimuth, and the peak interaction effects are shown in Fig. 9 in the form of instantaneous surface pressure distributions measured around $\psi = 180°$ azimuthal position.

The present Euler results are in very good agreement with both the experimental data (Ref. 18) and a previous two-dimensional Navier-Stokes calculation (Ref. 6). As seen from Fig. 9a for $\psi = 178.15,°$ the lift on the blade, which is initially zero in the absence of vortex interaction, is negative (because of the sense of rotation of the vortex) and gradually becomes positive as the blade passes the line vortex. This crossover of lift,

18

from negative to positive, seems to occur when the vortex is approximately aligned with the quarter-chord line of the blade (corresponding to $\bar{x}_v = 0.0$). As mentioned before, the two-dimensional approximation of this three-dimensional, unsteady interaction is, in fact, a very good assumption for this subcritical flow condition. The close agreement of the viscous and inviscid results suggests that the viscous effects are unimportant for this relatively weak interaction.

3.3.2 Supercritical Interaction

This case corresponds to the flow condition of $M_{tip} = 0.8$, $\mu = 0.2$, and $C_k\widehat{\Gamma} = 0.177$ at a blade reference station of $r_B = 0.893$. The interacting vortex location is same as in subcritical case. This flow condition, in constrast to the subcritical flow condition, exhibits strong unsteady time-lag effects in shock wave growth and decay for the advancing rotor. This feature seems to accentuate the three-dimensional nature of the flow and a two-dimensional approximation of this flow over predicts the shock wave strength and location as demonstrated in Ref. 6.

As before, to calculate the BVI flowfield, the interacting vortex is initialized at about $\psi = 120°$ azimuthal position and the time evolution of the flow is monitored as the blade advances in azimuth. Figures 10-11 show the interaction flowfield results in terms of instantaneous surface pressures for several azimuthal positions of the blade for the Euler and the Navier-Stokes calculations. Also shown in these figures are the experimental data (Ref. 18). Comparison of the results shows that while the Euler results (Fig. 10) have good agreement with the experimental data for all azimuthal locations of the blade, the Navier-Stokes results (Fig. 11) show only a qualitative agreement with the experimental data. This feature is strongly dependent on the accuracy of the base-line solution at the azimuthal location where the vortex is initialized. The vortex is intialized at the $\psi = 120°$ position of the blade for this case. Comparison of surface pressures of Fig. 4d at this location for the Navier-Stokes and Euler calculations shows that the

Euler results have better agreement with experiments than the Navier-Stokes results. Although the Euler grid is very coarse, it seems to capture the essential details of the flow sharply including the shock waves. Since the Navier-Stokes grid is too coarse, the shocks appear smeared. Nevertheless, it captures the essential qualitative features of the flow.

The effect of vortex interaction is to induce time dependent aerodynamic forces on the rotor. For example, as seen from the surface pressure plots of Figs. 10-11, the lift on the blade, which is intially zero, becomes negative (because of the sense of rotation of vortex) due to induced downwash and gradually increases to a positive value as the blade passes the fixed vortex. The peak effects of the interaction appear to occur when the blade leading edge is approximately above the line vortex.

3.4 Oblique Blade-Vortex Interaction

This case corresponds to a free stream condition of $M_{tip} = 0.763$ and $\mu = 0.197$. The interacting vortex located at $x_o = -2.13$ and $z_o = -0.25$ has a strength of $C_k \widehat{\Gamma} = 0.179$ for the reference blade section at $r_B = 0.946$. In contrast to the parallel interaction, the oblique interaction occurs over a larger azimuthal sweep of the rotor blade starting in first-quadrant and completing in second-quadrant. The peak interaction occurs at around $\psi = 20°$ in the first-quadrant and around $\psi = 160°$ in the second-quadrant. Therefore, the vortex is initialized at $\psi = 0.0°$ and the evolution of the unsteady interacting flow is monitored for the advancing rotor.

Figures 12-13 show the surface pressure distributions for several azimuthal positions of the blade from the Euler and the Navier-Stokes calculations of the interaction flowfield. As observed before, the transonic Euler calculations agree better with the experimental data[3] than the Navier-Stokes calculations for the reasons cited earlier. On the other hand, the interaction in the first-quadrant occurs at subcritical flow condition

20

and therefore the agreement of both the Euler and Navier-Stokes calculations with the experimental data is good at $\psi = 50°$. For the interaction in the second-qudrant, where the flow is supercritical, the Euler results have better agreement with the experiments than the Navier-Stokes results. Compared to the preceding transonic *parallel* interaction results, the Navier-Stokes results for this interaction appear to agree better with the experimental data. This is in direct consequence of the better agreement of the rotor-alone Euler and the Navier-Stokes surface pressures at all azimuthal positions, as seen in Fig. 12 for this flow condition. The maximum relative blade tip speed in this case (for $\psi = 90°$ position) is 0.91 compared to a value of 0.96 corresponding to the transonic parallel interaction case and is thus a weaker interaction.

From the surface pressures of Fig. 13, it can be seen that the lift on rotor blade, which is initially zero, becomes negative due to the vortex influence (because of the sense of rotation), increases to a maximum (negative) value in second-quadrant, and changes over to a positive value at about $\psi = 165°$ azimuthal position of the blade. The peak interaction appears to occur around the $\psi = 160°$ azimuthal position.

3.5 Lifting Hovering Rotor Flowfield

This section presents the steady solutions of a lifting hovering rotor. The flowfield of a hovering rotor can be either steady or unsteady depending on the reference frame of the observer. It is steady if the observer is fixed to the blade and riding with it. On the other hand, if the observer is stationed in the inertial reference frame, the flowfield appears unsteady. To take advantage of the steady state of the flowfield, a variable time-step option (see Ref. 31) is used to accelerate the convergence criteria of the numerical system. Rest of the features of the physical problem including the unsteady metrics are identical to the first problem presented above. The major advantage in this steady state problem is that the blade need not be physically advanced at each time step

21

The test cases selected for calculations correspond to the experimental test conditions of a two-bladed rigid rotor (Ref. 20). The rectangular blades of this rotor are made up of NACA 0012 airfoil sections and have an aspect ratio of 6. The blades are untwisted and untapered as before. Three typical sets of conditions are considered representing subcritical and supercritical tip speeds with two different collective pitches. The Reynolds number variation in these sets range from 1.92 to 3.83 million based on the tip speeds. In the calculation procedure, the flowfield is initially quiescent and the evolution of the flowfield is monitored as the blade is set in motion.

Figures 14-18 show steady surface pressure distributions for the subcritical case of $M_{tip} = 0.44$ with a collective pitch of 8° and a flow Reynolds number based on the tip speed of 1.92×10^6 at various radial stations along the blade. The solid line which is the present calculations shows excellent agreement with the experimental data (Ref. 20) at all radial stations. Also shown in these is a previous Navier-Stokes calculation of Srinivasan and McCroskey (Ref. 21) that used a simple wake model to bring-in the influence on the wake. Although there is good qualitative agreement between these two, the present calculation, which does not use any *ad hoc* assumptions on the wake and its influence, are in very good agreement with the experimental data. The two calculations are done on a comparable size grids but have different grid topologies.

The present wake capture calculations are atleast 5 times cheaper in computer time requirements compared to the one presented in Ref. 21. Calculations have also been done on a smaller grid, which was 1/8 the size of the present grid of about a million point, and the results show very good agreement with experiments even on this. The deficiency is in the inboard part of the blade where the grid is not very fine. The calculations on the smaller grid takes typically less than one hour on Cray2 supercomputer. This time is comparable to even many potential flow codes (Refs. 32-34) that are in use today.

Figures 19-22 show steady surface pressures for the supercritical case of M_{tip}

22

= 0.877 with a collective pitch of 8° and corresponding Reynolds number of 3.83×10^6. The surface pressures are shown for four radial stations and are compared with the experimental data of Caradonna and Tung (Ref. 20) and the Navier-Stokes calculations of Srinivasan and McCroskey (Ref. 21). As seen in these figures, the present wake capture Navier-Stokes results are in much better agreement with the experimental data than the Navier-Stokes results of Ref. 21. These results further demonstrate the superiority of this present methodology in predicting accurate results with out any *ad hoc* inputs to describe the wake which is an important influence in the lifting hovering rotor flowfields.

Figures 23-27 show surface pressures for the conditions of $M_{tip} = 0.877$, collective pitch of 12°, and flow Reynolds of 3.55×10^6. These calculations are done on the coarser grid. The results show only reasonable agreement with the experimental data. This is a severe case in terms of vorticity in the wake. These results are in similar agreement with experimental data as some of the potential flow methods that use wake models (Ref. 33-34). It should be emphasised that the present calculations, with the smaller grid, takes less than one hour of computer time on a supercomputer and no additional inputs are made to describe the wake.

4. CONCLUDING REMARKS

The research presented here address two related problems of a helicopter rotor and are therefore three-dimensional, unsteady and viscous dominated. For the first problem considered here, a numerical procedure is presented to calculate the unsteady, viscous and inviscid, three-dimensional flowfields of a helicopter rotor in forward flight and parallel and oblique blade-vortex interactions in subcritical and supercritical flow conditions. Important flow features such as unsteady time-lag effects in shock wave growth and evential decay, as well as the importance of three-dimensional effects are discussed. While it is possible to approximate the parallel blade-vortex interaction as two-dimensional and unsteady when the entire flow is subcritical, this same problem under supercritical flow condition and also the oblique blade-vortex interaction are naturally three-dimensional, and unsteady and has to be treated that way without any simplifications.

The numerical results are compared with two-sets of test data generated by Caradonna et al. (Refs. 18-19) on a model two-bladed rigid rotor in a wind tunnel. While the Euler results have good agreement with experiments, the Navier-Stokes results, with a very coarse grid, have only a good qualitative agreement. Nevertheless, the study demonstates that the numerical methodology presented here is capable of calculating accurately the flowfield of a helicopter rotor including the effects of vortex interaction under subcritical and supercritical flow conditions.

The second problem considered is that of a lifting hovering rotor flowfield. In contrast to the currently available potential flow methods that use wake modeling to do these flowfield calculations, the Navier-Stokes method presented here uses no *ad hoc* inputs to describe the wake. The wake and its influence are captured as a part of the overall flow field solution. The method is very fast and robust and is applicable to arbitrary blade planforms and geometries with out any modifications. The calculations

performed in this report for subcritical and supercritical flow conditions show excellent agreement with the experimental data.

5. REFERENCES

1. Srinivasan, G. R., McCroskey, W. J., Baeder, J. D., and Edwards, T. A., "Numerical Simulation of Tip Vortices of Wings in Subsonic and Transonic Flows", AIAA Journal, Vol. 26, No. 10, October 1988, pp. 1153-1162.

2. Workshop on Blade-Vortex Interactions (unpublished), NASA Ames Research Center, Moffett Field, California, October 1984.

3. Rai, M. M., "Navier-Stokes Simulation of Blade-Vortex Interaction Using High-Order Accurate Upwind Schemes", AIAA Paper 87-0543, January 1987.

4. Steinhoff, J. and Suryanarayanan, K., "The Treatment of Vortex Sheets in Compressible Potential Flow", AIAA Paper 83-1881-CP, July 1983.

5. Srinivasan, G. R. and McCroskey, W. J., "Numerical Simulations of Unsteady Airfoil-Vortex Interactions", VERTICA, Vol. 11, 1987, pp. 3-28.

6. Srinivasan, G. R., McCroskey, W. J., and Baeder, J. D., "Aerodynamics of Two-Dimensional Blade-Vortex Interaction", AIAA Journal, Vol. 24, No. 10, October 1986, pp. 1569-1576.

7. McCroskey, W. J. and Srinivasan, G. R., "Unsteady Interactions of Transonic Airfoils with Gusts and Concentrated Vortices", AGARD-CP-386, Unsteady Aerodynamics-Fundamentals and Applications to Aircraft Dynamics, November 1985, pp. S2.1 - S2.13.

8. Wu, J. C., Sankar, N. L., and Hsu, T. M., "Unsteady Aerodynamics of an Airfoil encountering a Passing Vortex", AIAA Paper 85-0203, January 1985.

9. Strawn, R. C. and Tung, C., "The Prediction of Transonic Loading on Advancing Helicopter Rotors", NASA TM-88238, April 1986.

10. Caradonna, F. X., Strawn, R. C., and Bridgeman, J.O., "An Experimental and Computational Study of Rotor-Vortex Interactions", paper presented at the Fourteenth European Rotorcraft Forum, Milano, Italy, September 1988.

11. Johnson, W., Helicopter Theory, Princeton University Press, 1980, Princeton, New Jersey.

12. Summa, J. M. and Clark, D. R., "A Lifting-Surface Method for Hover/climb Loads", 35th Annual Forum of the Americal Helicopter Society, Paper 79-1, Washington, DC, May 1979.

13. Kroll, N., "Computation of the Flow Fields of Propellers and Hovering Rotors Using Euler Equations", Proceedings of the Twelfth European Rotorcraft Forum, Garmisch-Partenkirchen, Federal Republic of Germany, September 1986.

14. Kramer, E., Hertel, J. and Wagner, S., "Computation of Subsonic and Transonic Helicopter Rotor Flow Using Euler Equations", Vertica, Vol. 12, No. 3, 1988, pp. 279-291.

15. Roberts, T. W., "Solution Method for a Hovering Helicopter Rotor Using the Euler Equations", AIAA Paper 85-0436, January 1985, Reno, Nevada.

16. Chen, C.-L. and McCroskey, W. J., "Numerical Simulation of Helicopter Multi-Bladed Rotor Flow", AIAA Paper 88-0046, January 1988, Reno, Nevada.

17. Steinhoff, J. S. and Ramachandran, K., "Free Wake analysis of Compressible Rotor Flow Fields in Hover", Paper No. 20, Twelfth European Rotorcraft Forum, Garmisch-Partenkirchen, Federal Republic of Germany, September 1986.

18. Caradonna, F. X., Laub, G. H., and Tung, C., "An Experimental Investigation of the Parallel Blade-Vortex Interaction", Paper presented at the 10th European Rotorcraft

Forum, The Hague, Netherlands, August 1984.

19. Caradonna, F. X., Lautenschlager, J., and Silva, M., "An Experimental Study of Rotor Blade-Vortex Interactions", AIAA Paper 88-0045, January 1988.

20. Caradonna, F. X. and Tung, C., "Experimental and Analytical Studies of a Model Helicopter Rotor in Hover", NASA Technical Memorandum - 81232, September 1981; also Vertica, Vol. 5, No. 2, 1981, pp. 149-161.

21. Srinivasan, G. R. and McCroskey, W. J., "Navier-Stokes Calculations of Hovering Rotor Flowfields", Journal of Aircraft, Vol. 25, No. 10, October 1988, pp. 865-874.

22. Pulliam, T. H. and Steger, J. L., "Implicit Finite-Difference Simulations of Three-Dimensional Compressible Flow", AIAA Journal, Vol. 18, No. 2, February 1980, pp. 159-167.

23. Baldwin, B. S. and Lomax, H., "Thin Layer Approximation and Algebraic Model for Separated Turbulent Flow", AIAA Paper 78-257, January 1978.

24. Isom, M. P., "Unsteady Subsonic and Transonic Potential Flow Over Helicopter Rotor Blades", NASA CR-2463, October 1974.

25. Ying, S. X., Steger, J. L., Schiff, L. B., and Baganoff, D., "Numerical Simulation of Unsteady, Viscous, High-Angle-Of-Attack Flows Using a Partially Flux-Split Algorithm", AIAA Paper 86-2179, August 1986.

26. Steger, J. L. and Warming, R. F., "Flux Vector Splitting of the Inviscid Gasdynamic Equations with Application to Finite-Difference Methods", J. of Comp. Phys., Vol. 40, No.2, 1981, pp.263-293.

27. Steger, J. L., Private Communication, University of California, Davis.

28. Obayashi, S., "Numerical Simulation of Underexpanded Plumes Using Upwind Algorithms", AIAA Paper 88-4360, AIAA Atmospheric Flight Mechanics Conference, August 1988, Minneapolis, Minnesota.

29. Steger, J. L. and Chaussee, D. S., "Generation of Body-Fitted Coordinates Using Hyperbolic Partial Differential Equations", SIAM J. Sci. Stat. Comput., Vol. 1, No. 4, December 1980, pp. 431-437.

30. Jameson, A. and Baker, T. J., "Solution of the Euler Equations for Complex Configurations", AIAA Paper 83-1929-CP, July 1983.

31. Srinivasan G. R., Chyu W. J. and Steger J. L., "Computation of Simple Three-Dimensional Wing-Vortex Interaction in Transonic Flow", AIAA Paper 81-1206, June 1981.

32. Ramachandran, K., Tung, C. and Caradonna, F. X., "Rotor Hover Performance Prediction Using a Free-Wake, Computational Fluid Dynamics Method", Journal of Aircraft, Vol. 26, No. 12, December 1989, pp. 1105-1110.

33. Strawn, R. C. and Caradonna, F. X., "Conservative Full-Potential Model for Unsteady Transonic Rotor Flows", AIAA Journal, Vol. 25, No. 2, February 1987, pp. 193-198.

34. Egolf, T. A. and Sparks, S. P., "A Full Potential Flow Analysis With Realistic Wake Influence for Helicopter Rotor Airload Prediction", NASA CR-4007, January 1987.
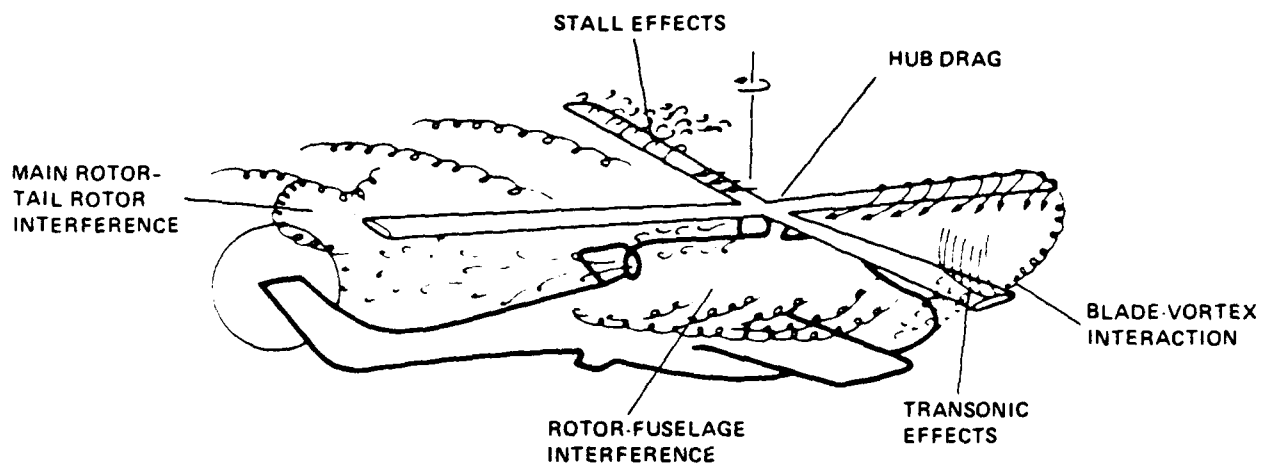
Fig. 1 Schematic of the complex flowfield of a helicopter rotor in forward flight.
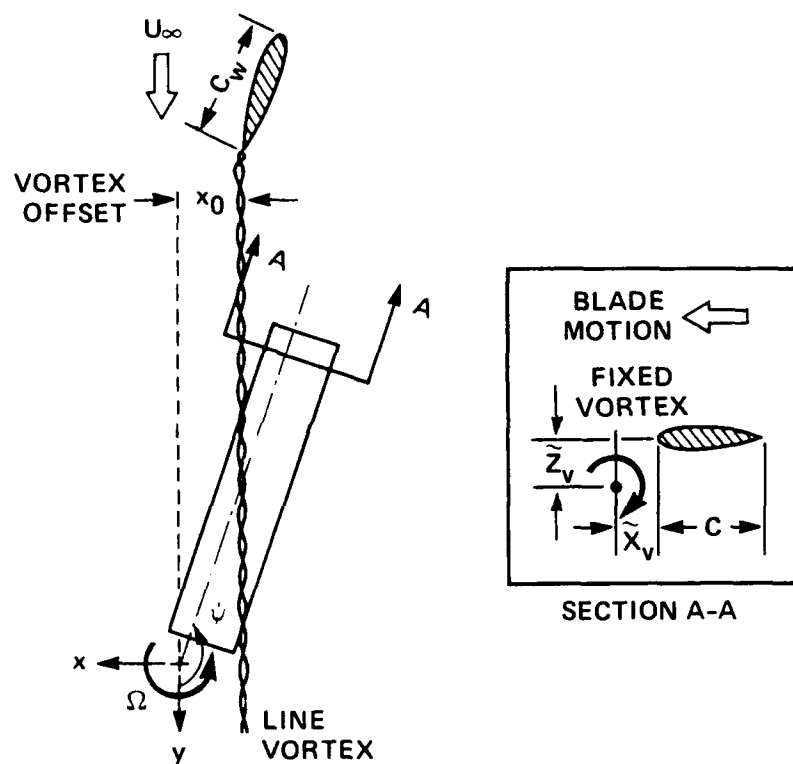
Fig. 2 Schematic of the rotor BVI wind tunnel test.
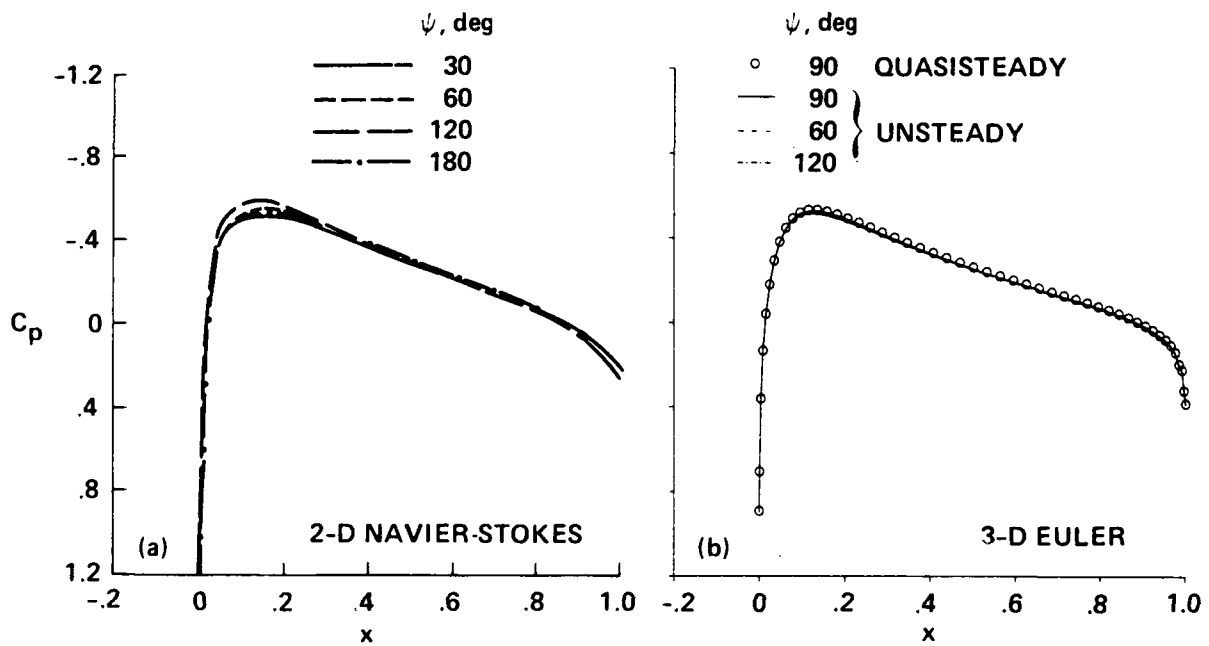
Fig. 3 Instantaneous surface pressure distributions at the reference blade section for advancing rotor. $M_{tip} = 0.6$, $\mu = 0.2$, Re = 2.1x10^6, $r_B = 0.893$.
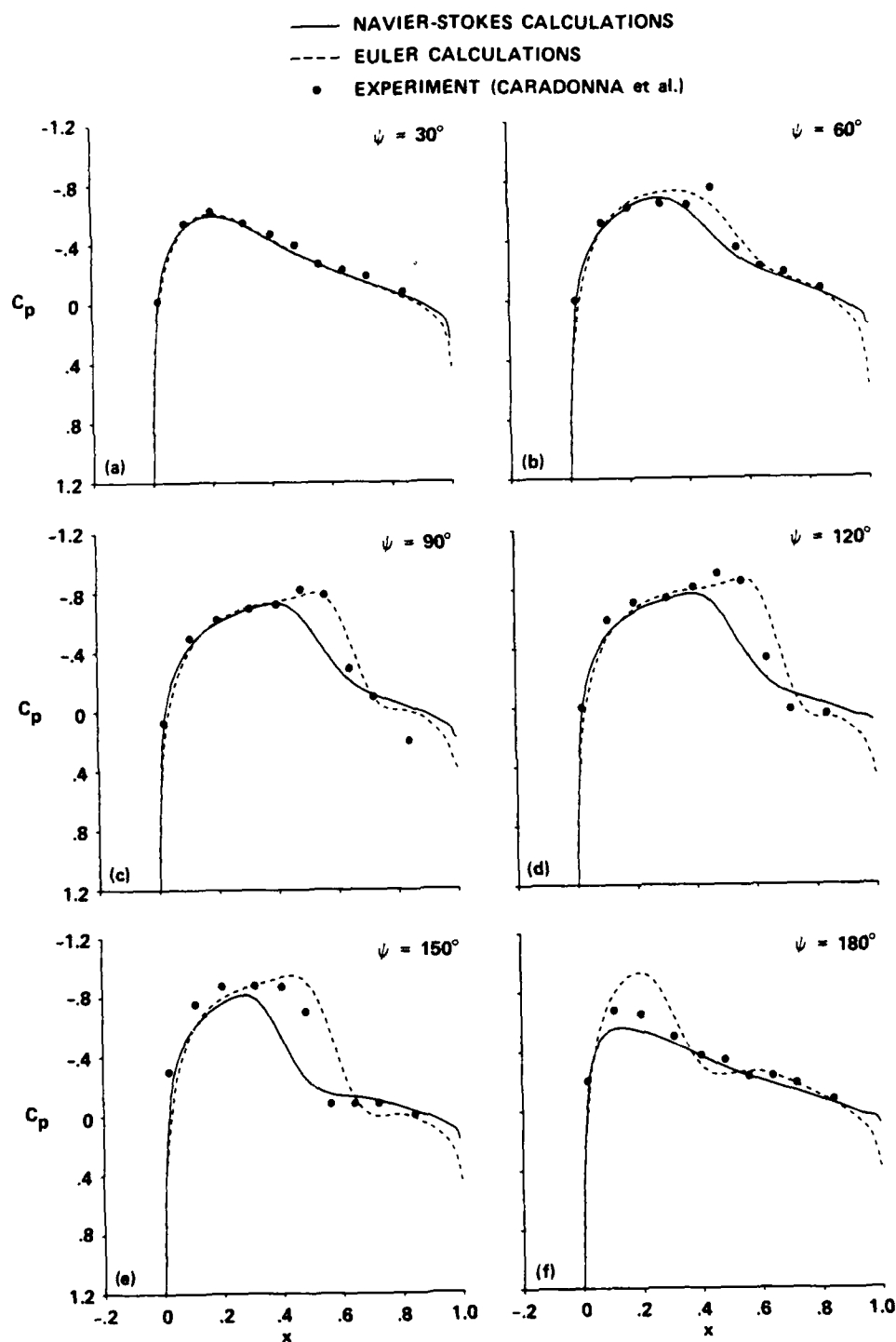
Fig. 4 Instantaneous surface pressure distributions at the reference blade section for advancing rotor. $M_{tip} = 0.8$, $\mu = 0.2$, Re = 2.89×10^6, $r_B = 0.893$.

33
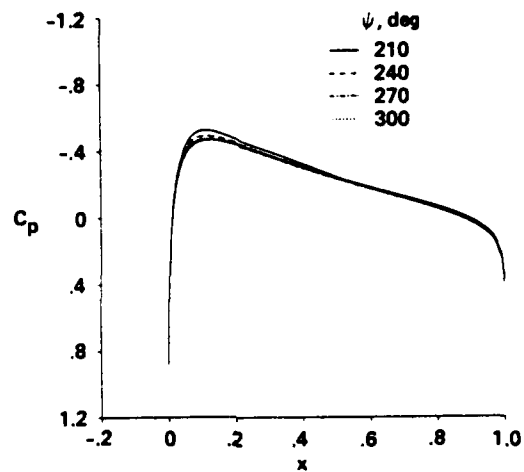
Fig. 5 Instantaneous surface pressure distributions at the reference blade section for retreating-blade-Euler solution. $M_{tip} = 0.8$, $\mu = 0.2$, $r_B = 0.893$.
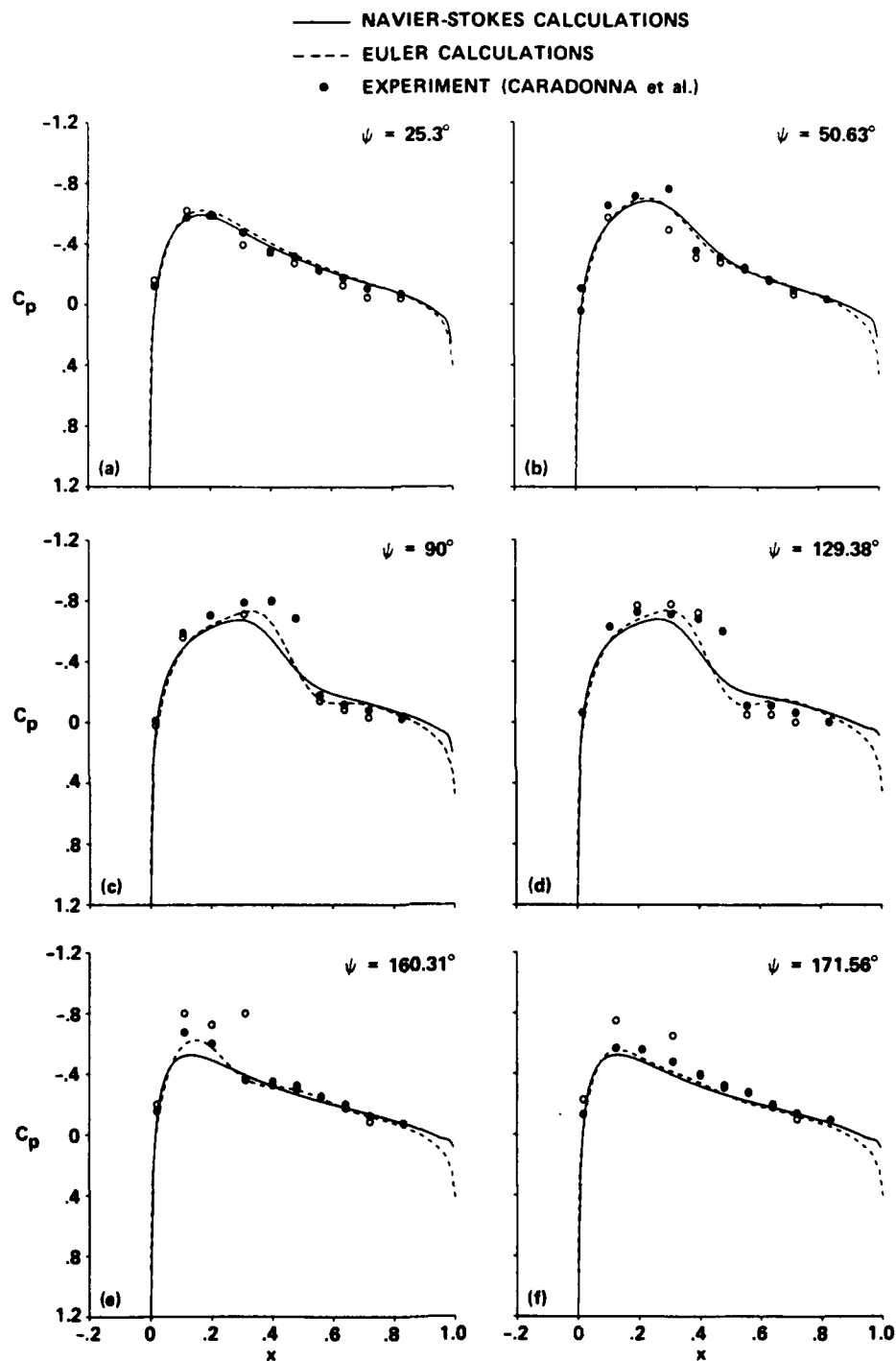
Fig. 6 Instantaneous surface pressure distributions at the reference blade section for advancing rotor. $M_{tip} = 0.763$, $\mu = 0.197$, Re $= 2.75\text{x}10^6$, $r_B = 0.946$.

35
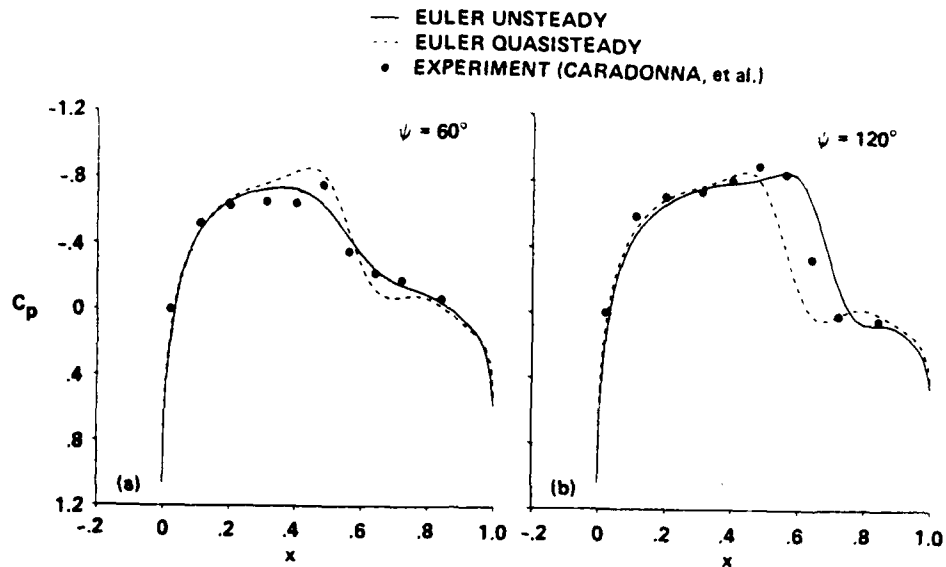
Fig. 7 Comparison of pressure distributions for quasi-steady and unsteady Euler calculations. $M_{tip} = 0.8$, $\mu = 0.2$, $r_B = 0.893$.
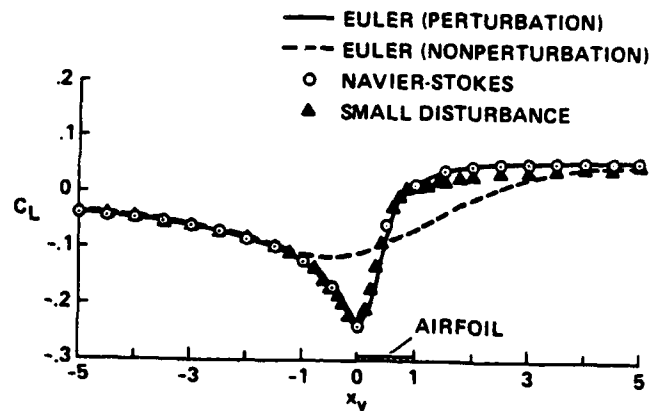
Fig. 8 Effectiveness of the prescibed-vortex method for two-dimensional BVI: NACA 64A006 airfoil. $M_\infty = 0.85$, $\widehat{\Gamma} = 0.2$, $z_o = -0.26$.
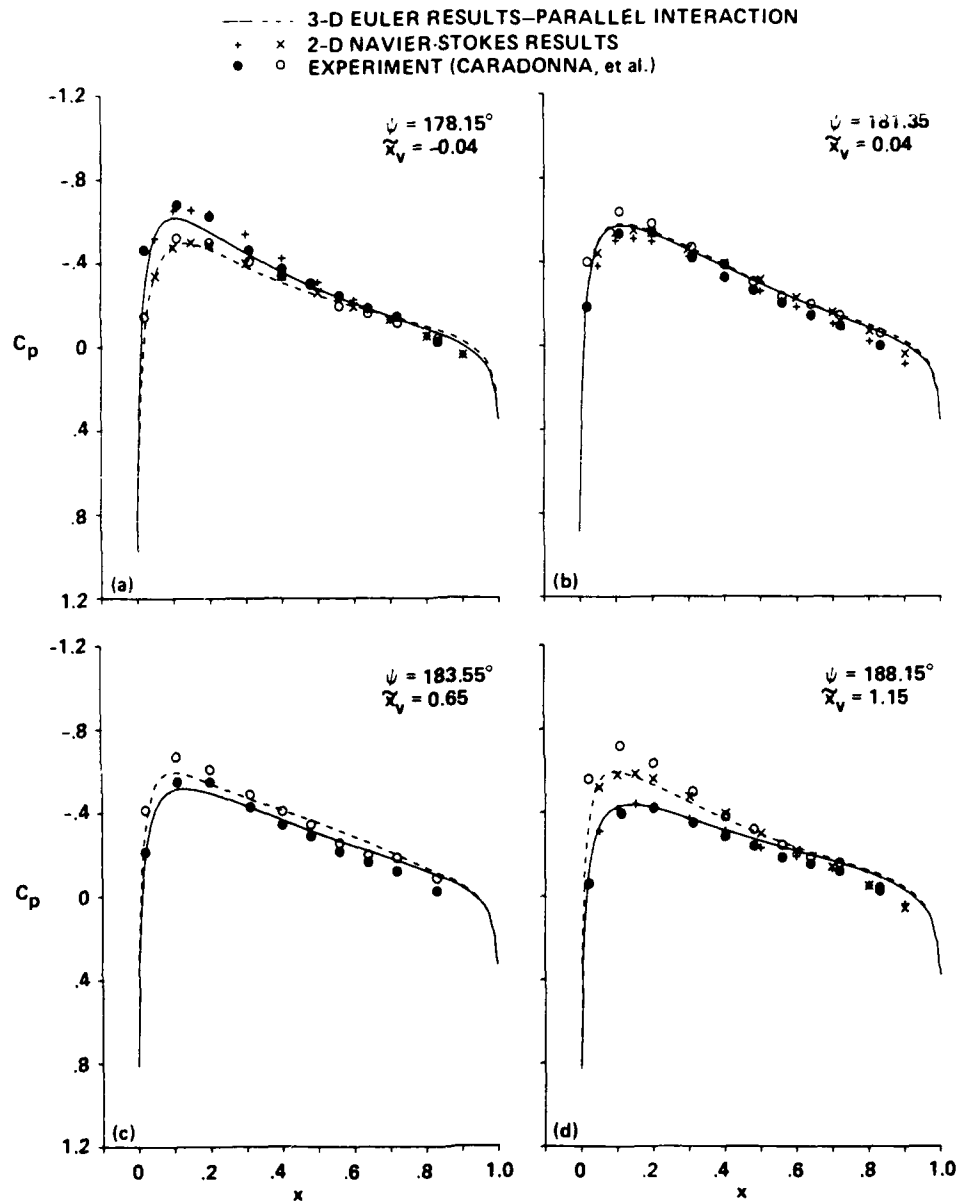
Fig. 9 Comparison of instantaneous surface pressures during subsonic parallel blade-vortex interaction. The solid line, the solid circle, and the symbol + refer to the vortex side of the blade. $M_{tip} = 0.6$, $\mu = 0.2$, $Re = 2.1 \times 10^6$, $\widehat{\Gamma} = 0.133$, $x_o = 0.0$, $z_o = -0.4$, $r_B = 0.893$.
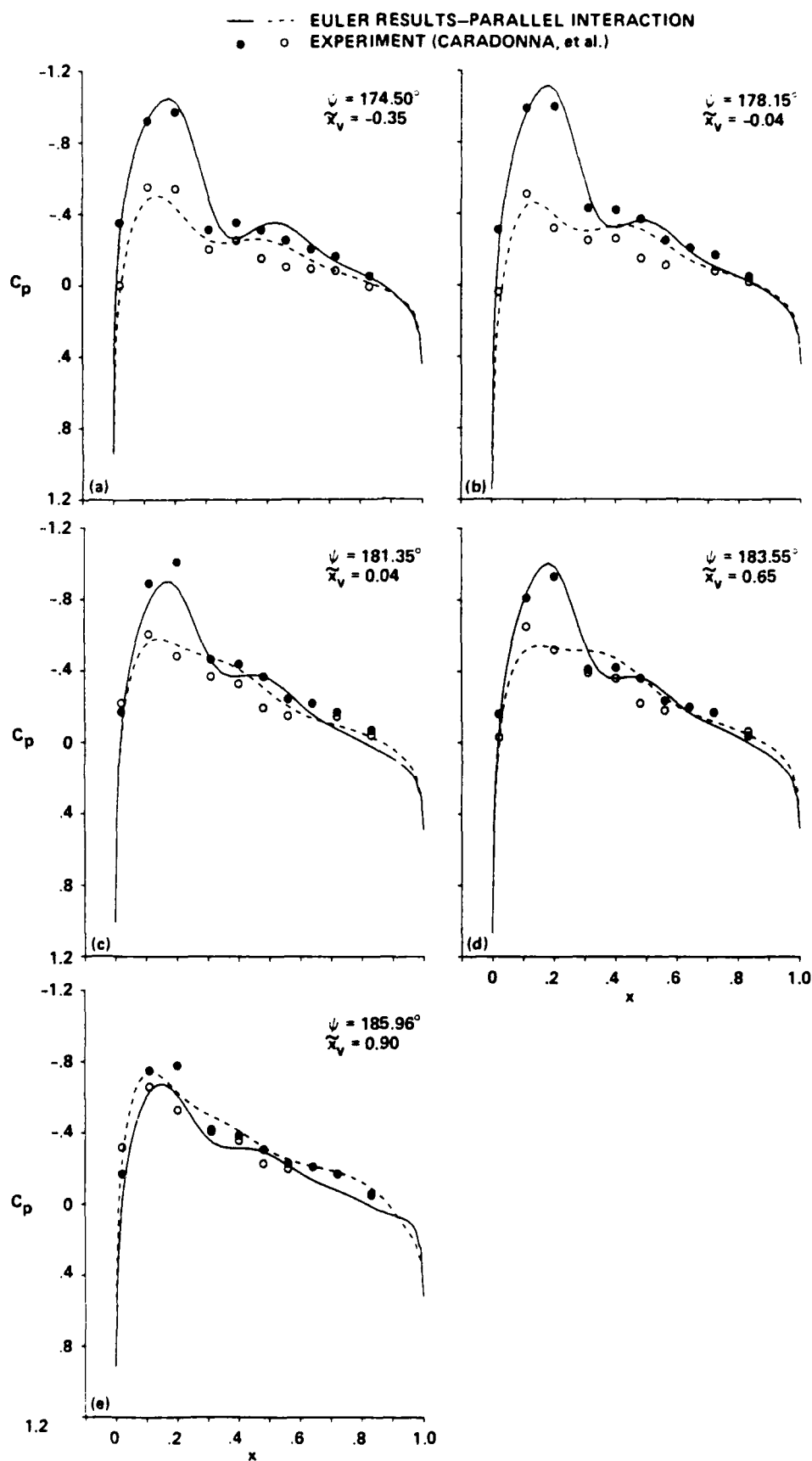
Fig. 10 Instantaneous surface pressures during transonic parallel blade-vortex interaction
- the Euler results. The solid line and the solid circle refer to the vortex side of the blade.
$M_{tip} = 0.8$, $\mu = 0.2$, $\widehat{\Gamma} = 0.177$, $x_o = 0.0$, $z_o = -0.4$, $r_B = 0.893$.

38
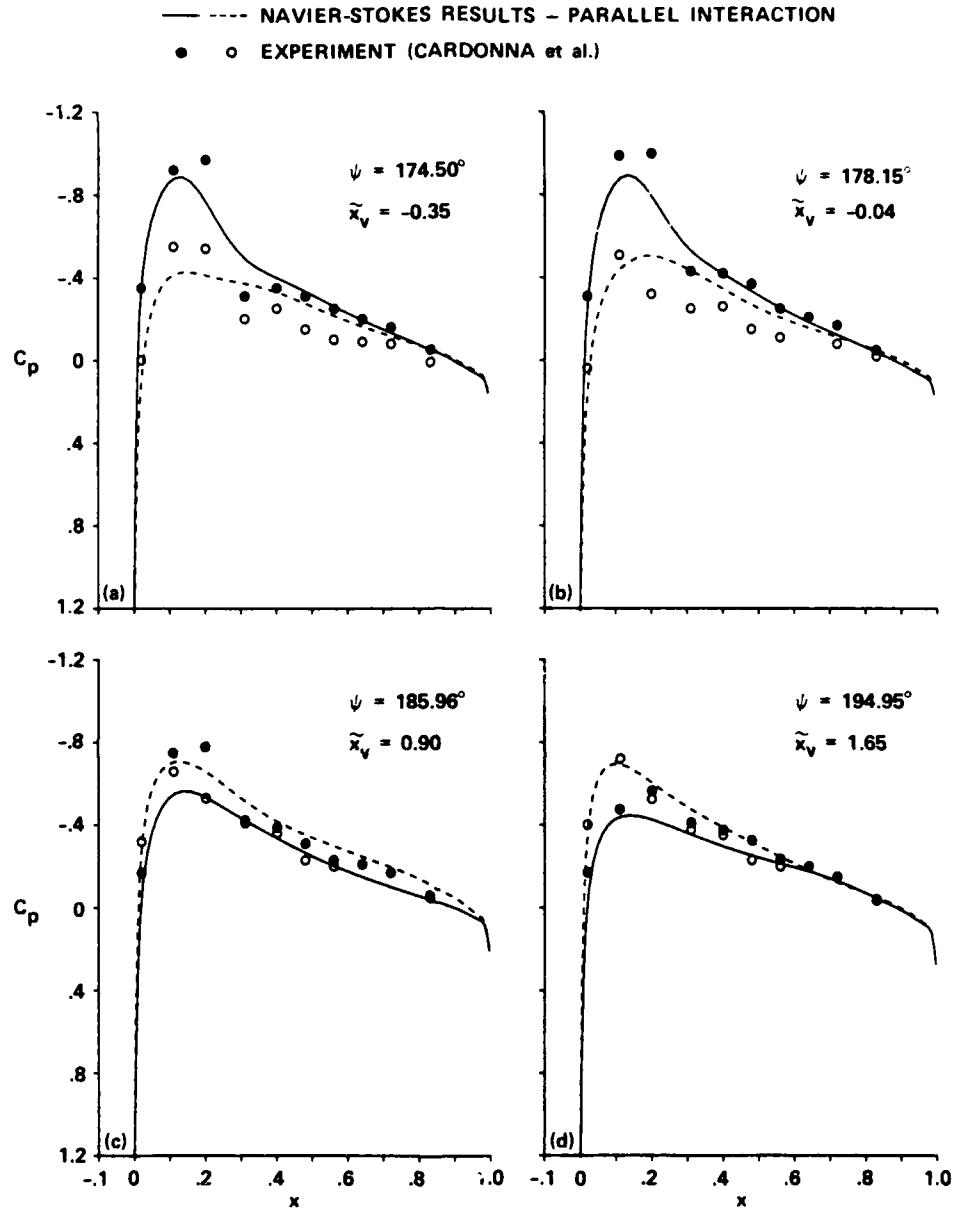
Fig. 11 Instantaneous surface pressures during parallel blade-vortex interaction - the Navier-Stokes results. The solid line and the solid circle refer to the vortex side of the blade. $M_{tip} = 0.8$, $\mu = 0.2$, Re $= 2.89 \times 10^6$, $\widehat{\Gamma} = 0.177$, $x_o = 0.0$, $z_o = -0.4$, $r_B = 0.893$.
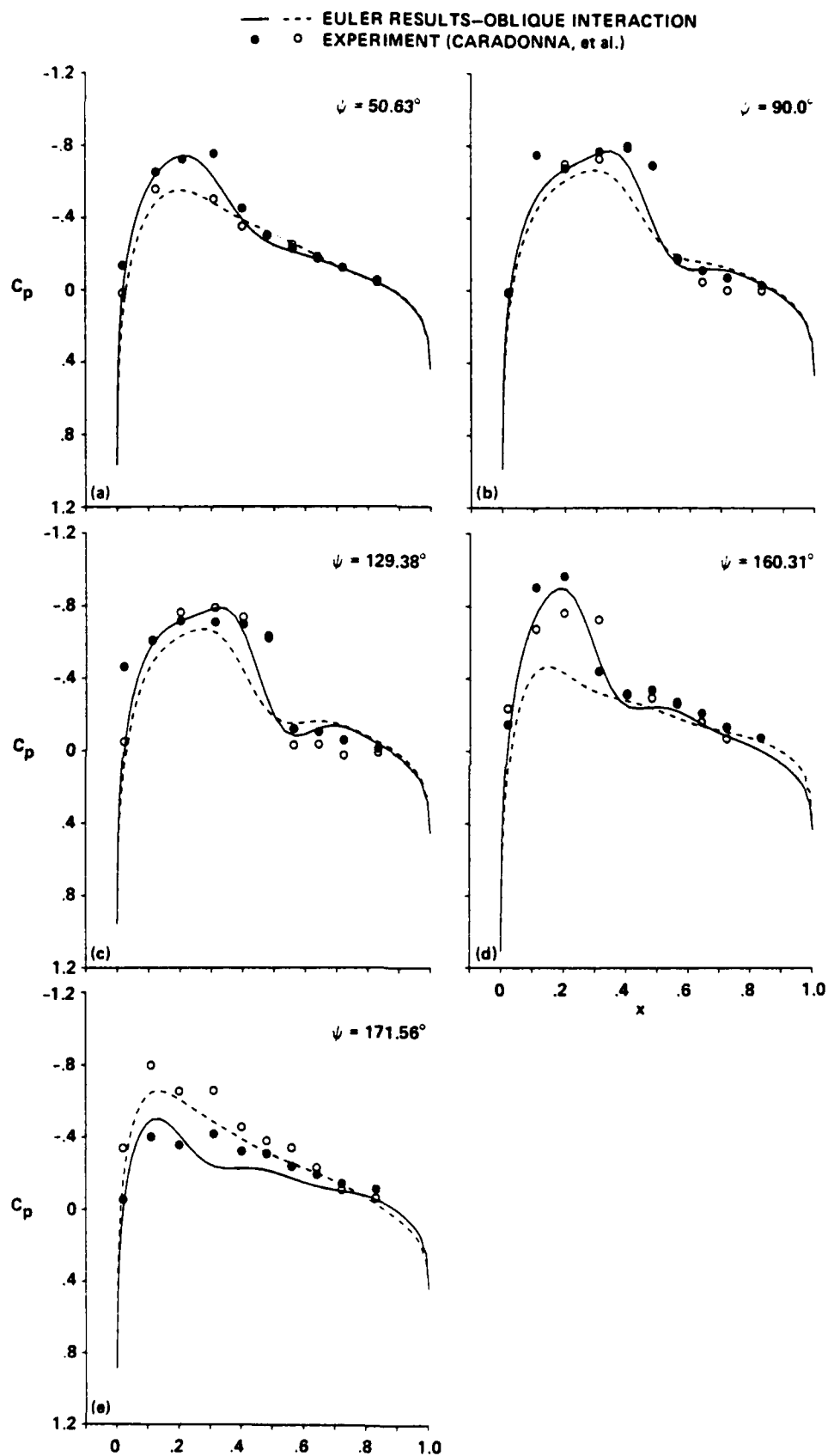
Fig. 12 Instantaneous surface pressures during oblique blade-vortex interaction - the Euler results. The solid line and the solid circle refer to the vortex side of the blade. $M_{tip} = 0.763$, $\mu = 0.197$, Re = 2.75x10^6, $\widehat{\Gamma} = 0.179$, $x_o = -2.13$, $z_o = -0.25$, $r_B = 0.946$.

Fig. 13 Instantaneous surface pressures during oblique blade-vortex interaction - the Navier-Stokes results. The solid line and the solid circle refer to the vortex side of the blade. $M_{tip} = 0.763$, $\mu = 0.197$, Re $= 2.75 \times 10^6$, $\widehat{\Gamma} = 0.179$, $x_o = -2.13$, $z_o = -0.25$, $r_B = 0.946$.

41

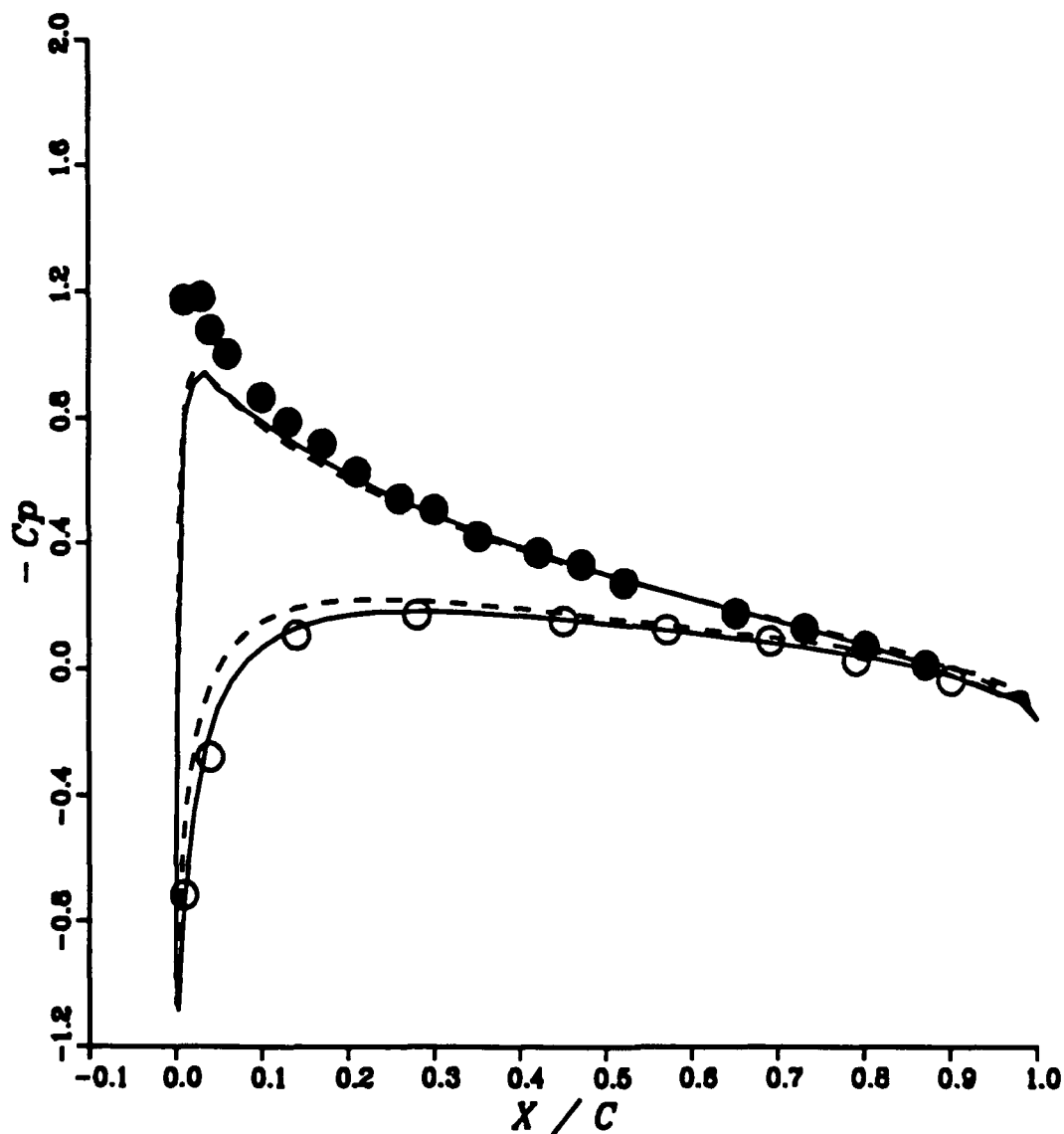|	M_{tip}	α_t	$2y/b$	
● ○	0.4400	8.0000	0.5000	Experiment–Caradonna and Tung
——	0.4400	8.0000	0.4924	Navier–Stokes Results – Present
– – –	0.4400	8.0000	0.4935	Navier–Stokes Results – Ref. 21
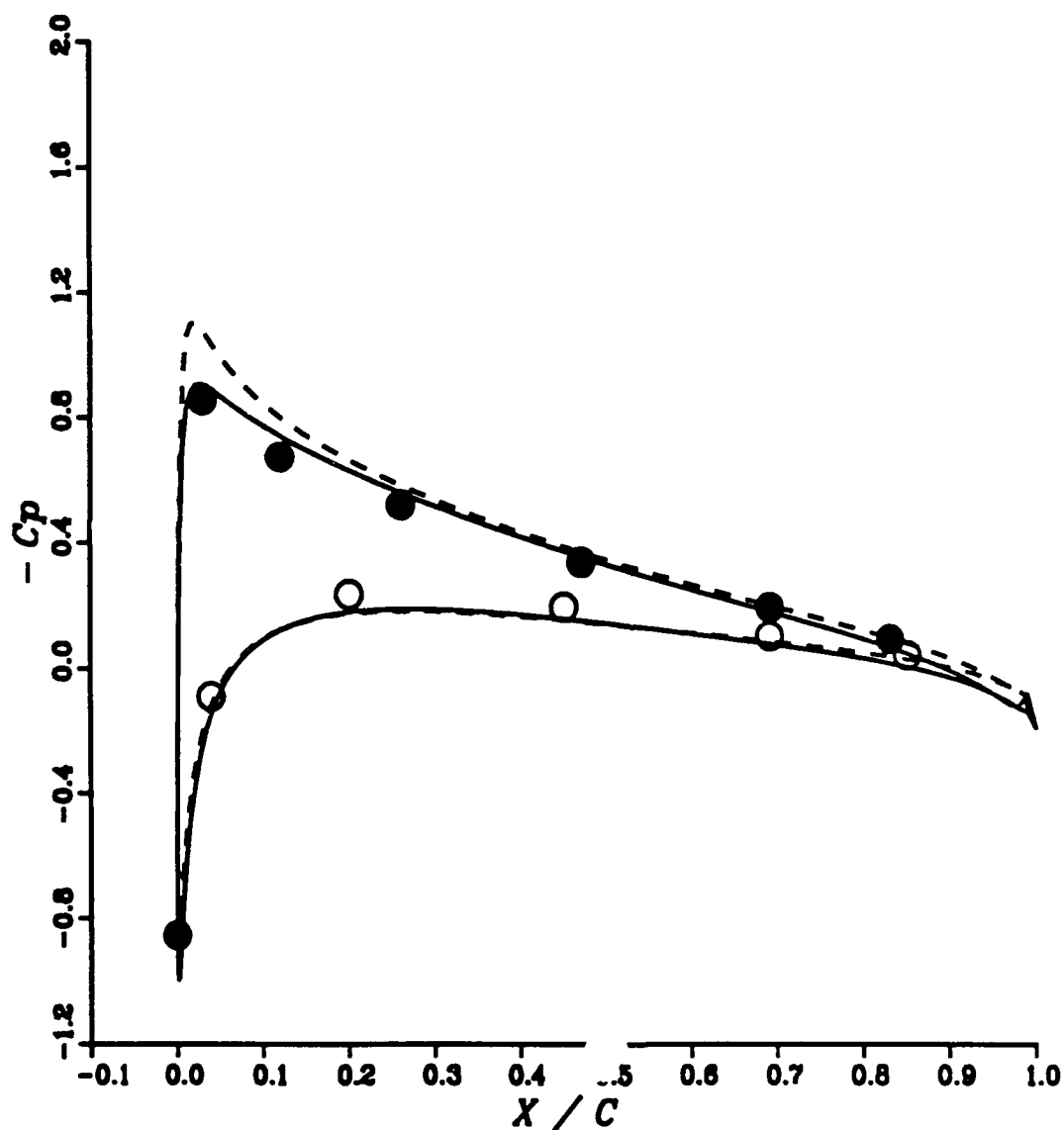
Fig. 14 Comparison of surface pressures for a lifting hovering rotor. $M_{tip} = 0.44$, $\alpha_t = 8°$, Re $= 1.92 \times 10^6$ and $r_B = 0.5$.

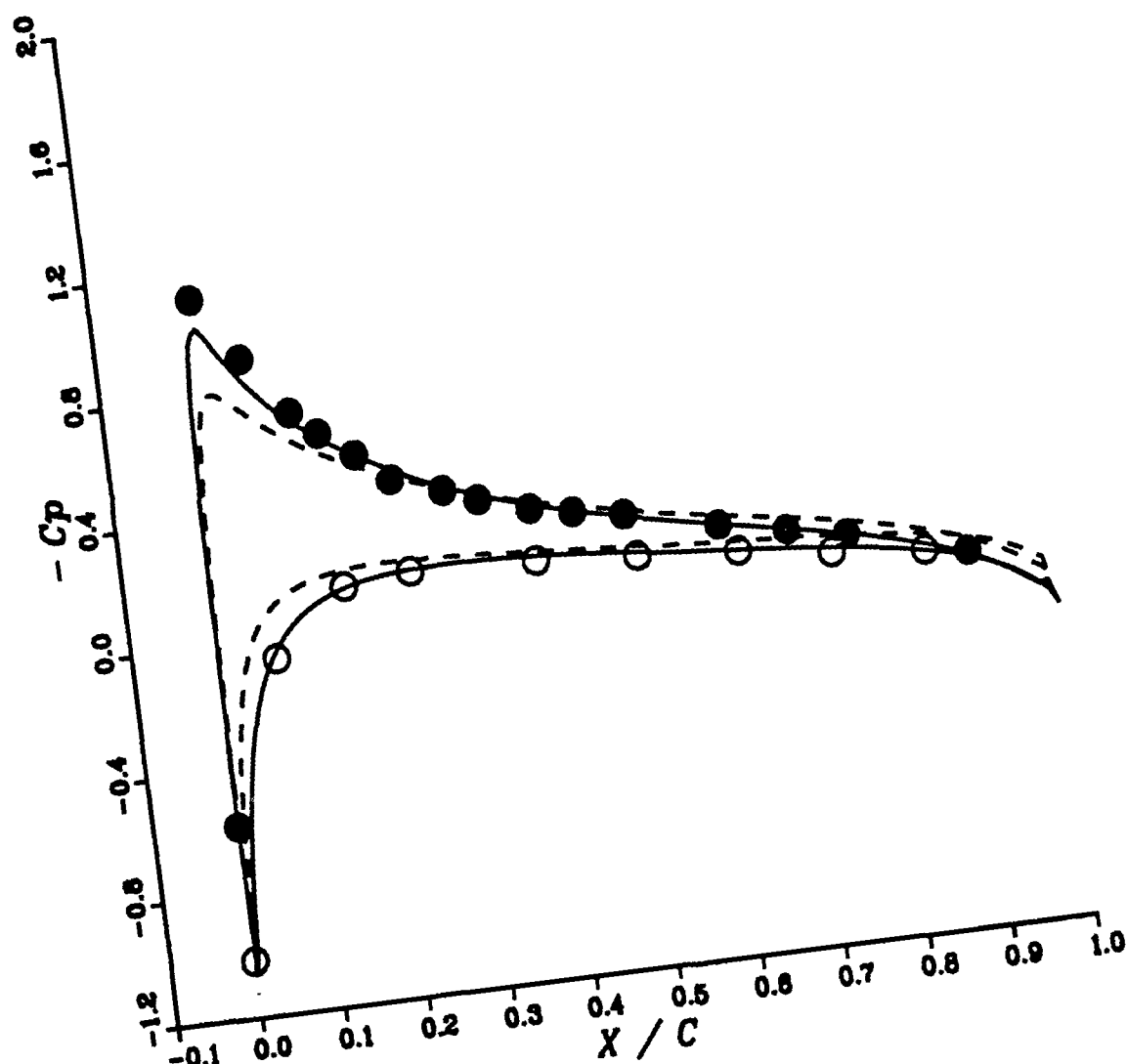|	M_{tip}	α_t	$2y/b$	
● ○	0.4400	8.0000	0.6800	Experiment–Caradonna and Tung
——	0.4400	8.0000	0.6881	Navier–Stokes Results – Present
- - -	0.4400	8.0000	0.6820	Navier–Stokes Results – Ref. [21]
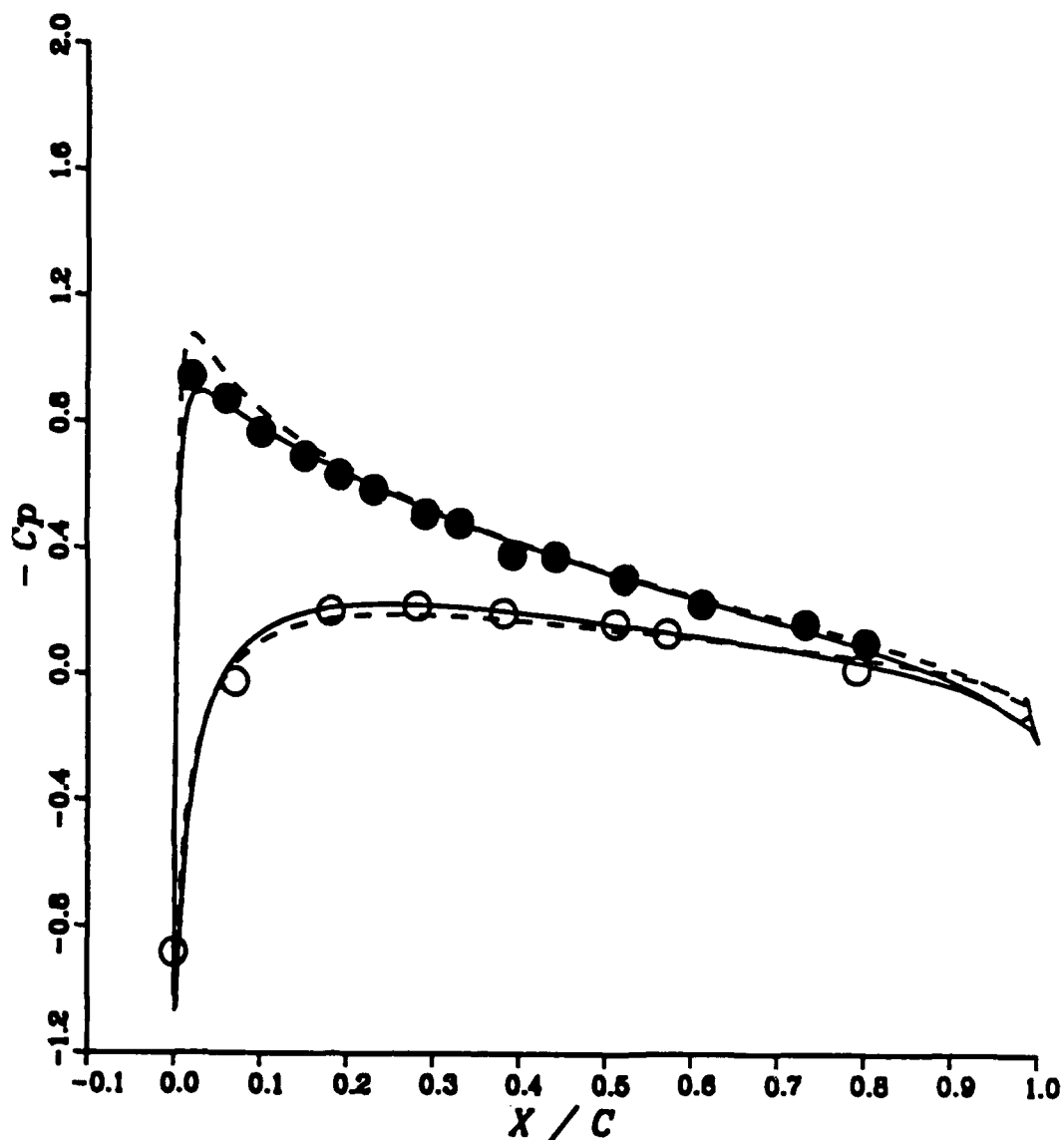
Fig. 15 Comparison of surface pressures for a lifting hovering rotor. $M_{tip} = 0.44$, $\alpha_t = 8°$, Re $= 1.92 \times 10^6$ and $r_B = 0.68$.

43
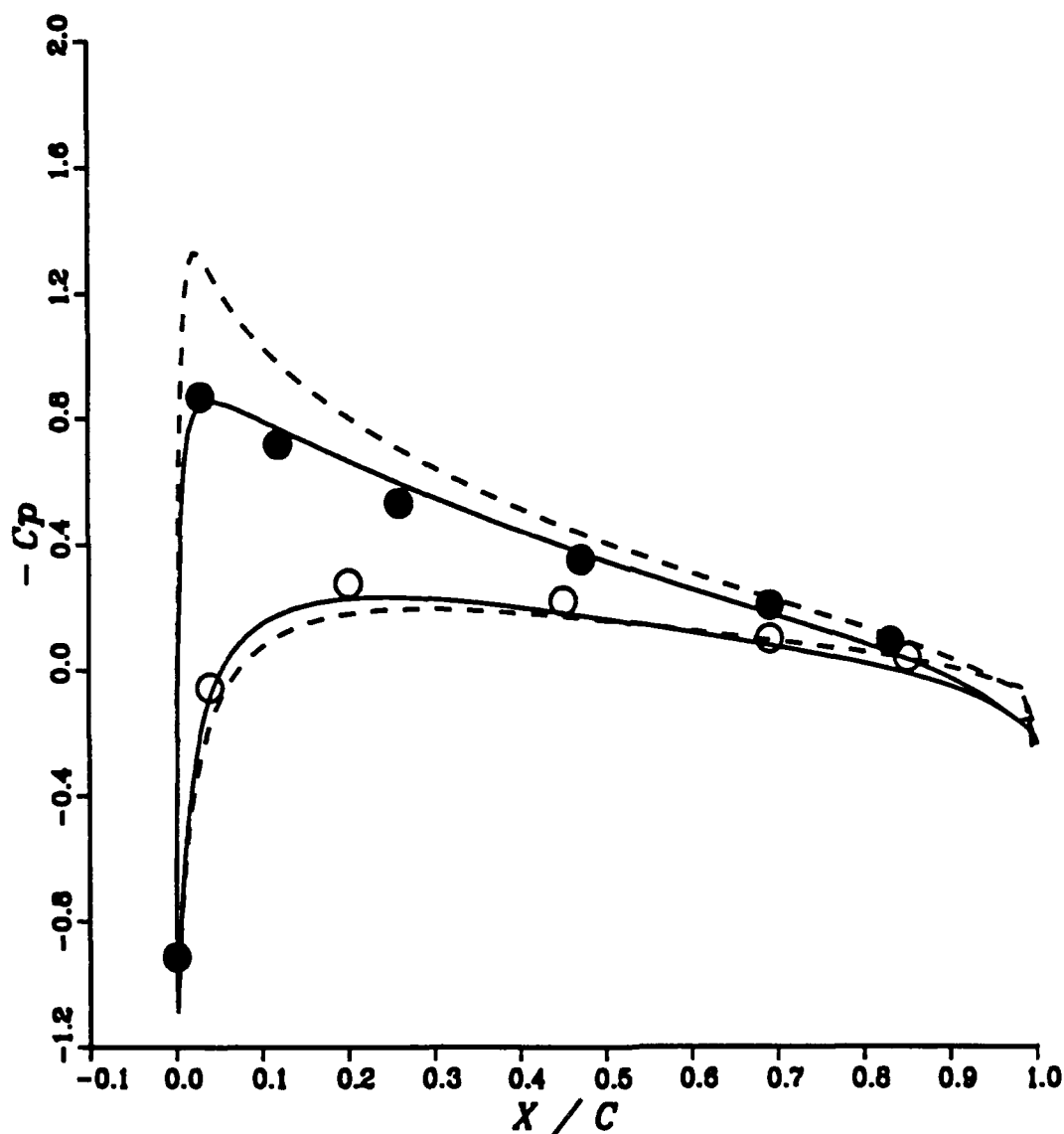
Fig. 16 Comparison of surface pressures for a lifting hovering rotor. $M_{tip} = 0.44$, $\alpha_t = 8°$, Re = 1.92×10^6 and $r_B = 0.80$.

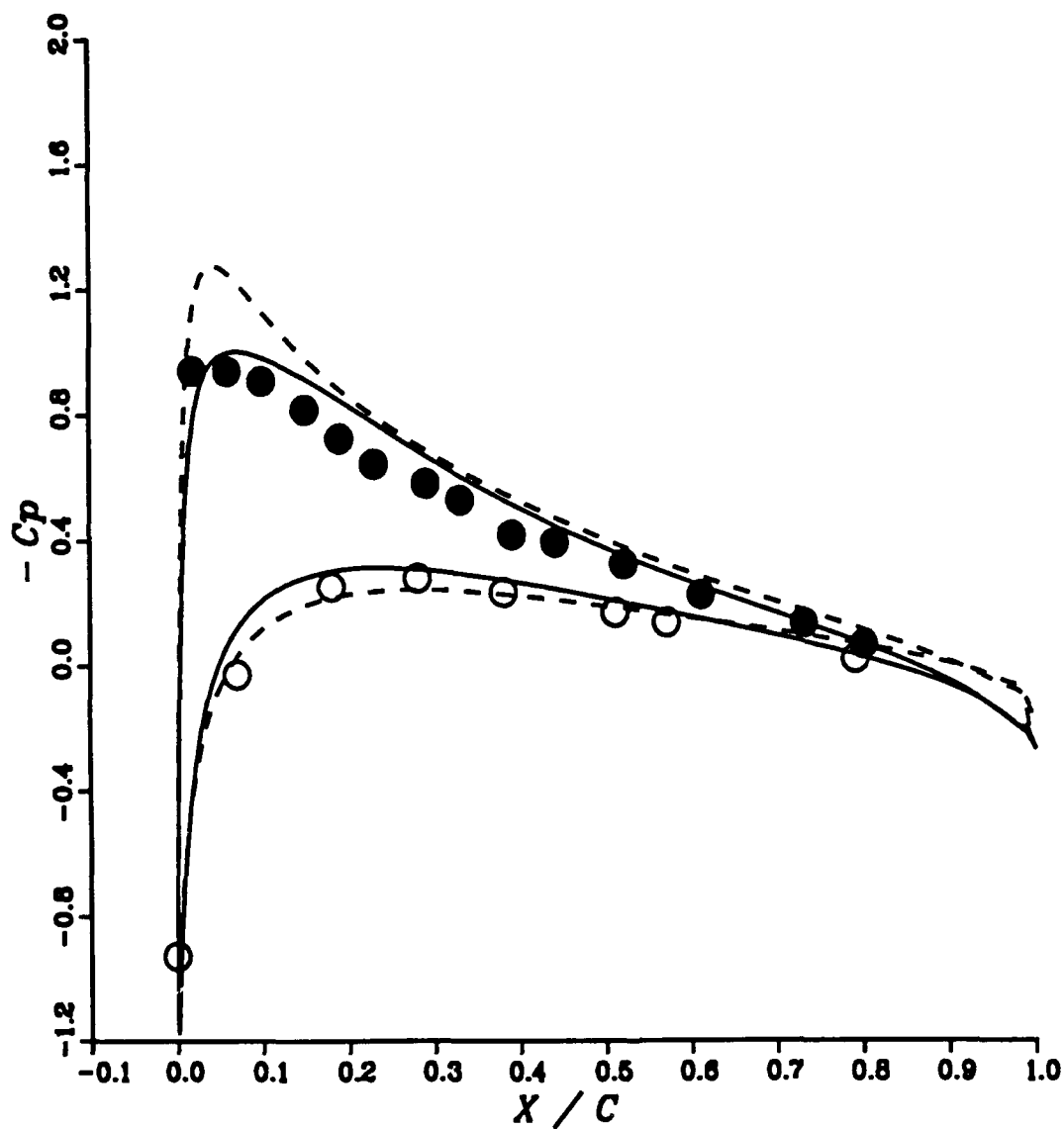|	M_{tip}	α_t	$2y/b$	
● ○	0.4400	8.0000	0.8900	Experiment–Caradonna and Tung
——	0.4400	8.0000	0.8899	Navier–Stokes Results – Present
- - -	0.4400	8.0000	0.8883	Navier–Stokes Results – Ref.21

Fig. 17 Comparison of surface pressures for a lifting hovering rotor. $M_{tip} = 0.44$, $\alpha_t = 8°$, Re $= 1.92\text{x}10^6$ and $r_B = 0.89$.

|	M_{tip}	α_t	$2y/b$	
● ○	0.4400	8.0000	0.9600	Experiment-Caradonna and Tung
——	0.4400	8.0000	0.9572	Navier–Stokes Results – Present
- - -	0.4400	8.0000	0.9576	Navier–Stokes Results – Ref. [21]

Fig. 18 Comparison of surface pressures for a lifting hovering rotor. $M_{tip} = 0.44$, $\alpha_t = 8°$, $Re = 1.92 \times 10^6$ and $r_B = 0.96$.

46

M tip	α_t	$2y/b$	
● ○	0.8770	8.0000	0.5000	Experiment–Caradonna and Tung
——	0.8770	8.0000	0.4924	Navier–Stokes Results – Present
– – –	0.8770	8.0000	0.5000	Navier–Stokes Results – Ref. [21]

Fig. 19 Comparison of surface pressures for a lifting hovering rotor. $M_{tip} = 0.877$, $\alpha_t = 8°$, Re $= 3.83 \times 10^6$ and $r_B = 0.5$.

| M_{tip}	α_t	$2y/b$	
● ○	0.8770	8.0000	0.6800	Experiment–Caradonna and Tung
——	0.8770	8.0000	0.6881	Navier–Stokes Results – Present
- - -	0.8770	8.0000	0.6953	Navier–Stokes Results – Ref. 21

Fig. 20 Comparison of surface pressures for a lifting hovering rotor. $M_{tip} = 0.877$, $\alpha_t = 8°$, Re = 3.83x10^6 and $r_B = 0.68$.

| M_{tip}	α_t	$2y/b$	
● ○ 0.8770	8.0000	0.8000	Experiment–Caradonna and Tung
—— 0.8770	8.0000	0.7966	Navier–Stokes Results – Present
- - - 0.8770	8.0000	0.8023	Navier–Stokes Results – Ref. 21
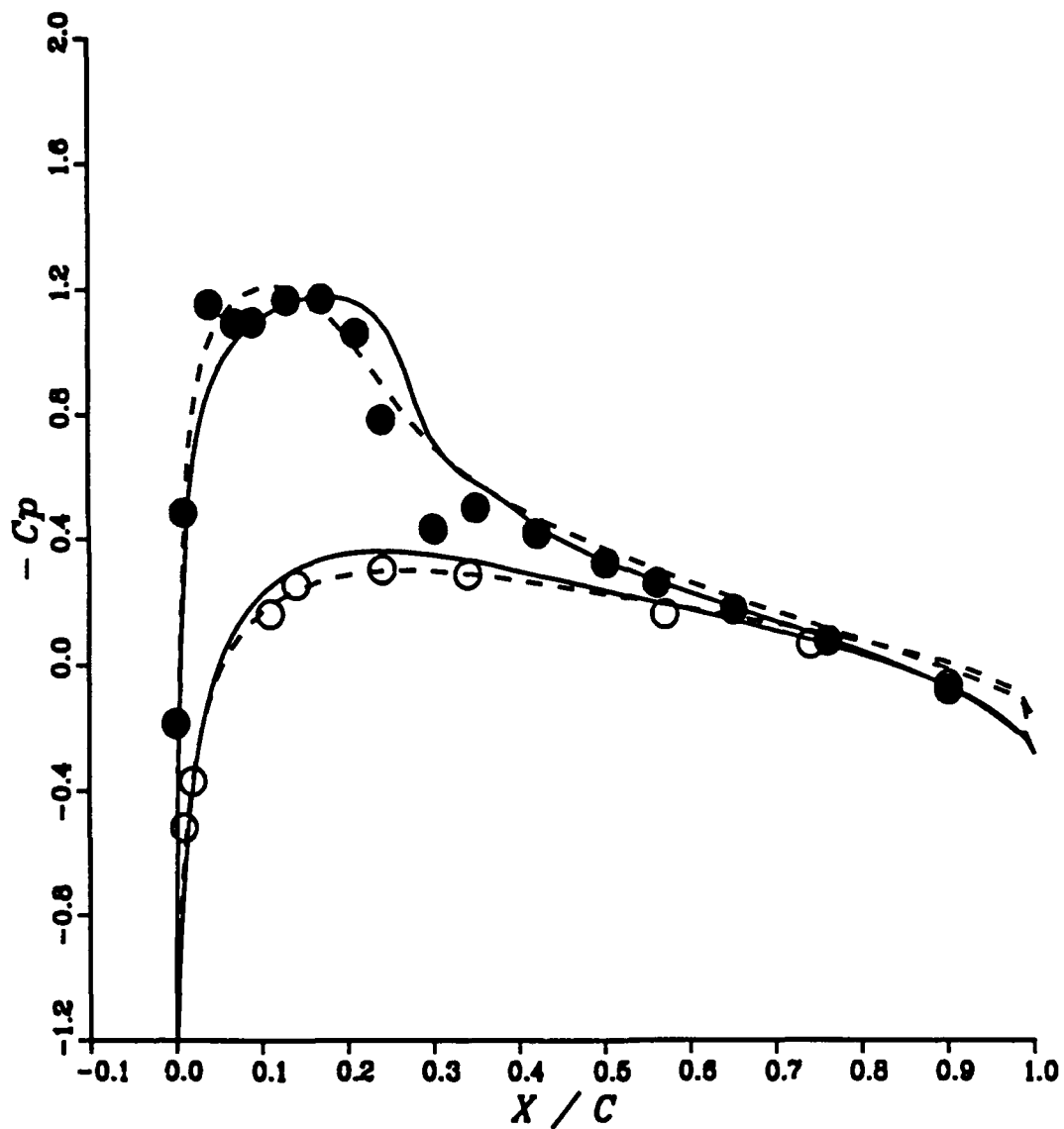
Fig. 21 Comparison of surface pressures for a lifting hovering rotor. $M_{tip} = 0.877$, $\alpha_t = 8°$, Re = 3.83x10^6 and $r_B = 0.80$.

	M_{tip}	α_t	$2y/b$	
● O	0.8770	8.0000	0.8900	Experiment–Caradonna and Tung
——	0.8770	8.0000	0.8899	Navier–Stokes Results – Present
- - -	0.8770	8.0000	0.8883	Navier–Stokes Results – Ref. [21]
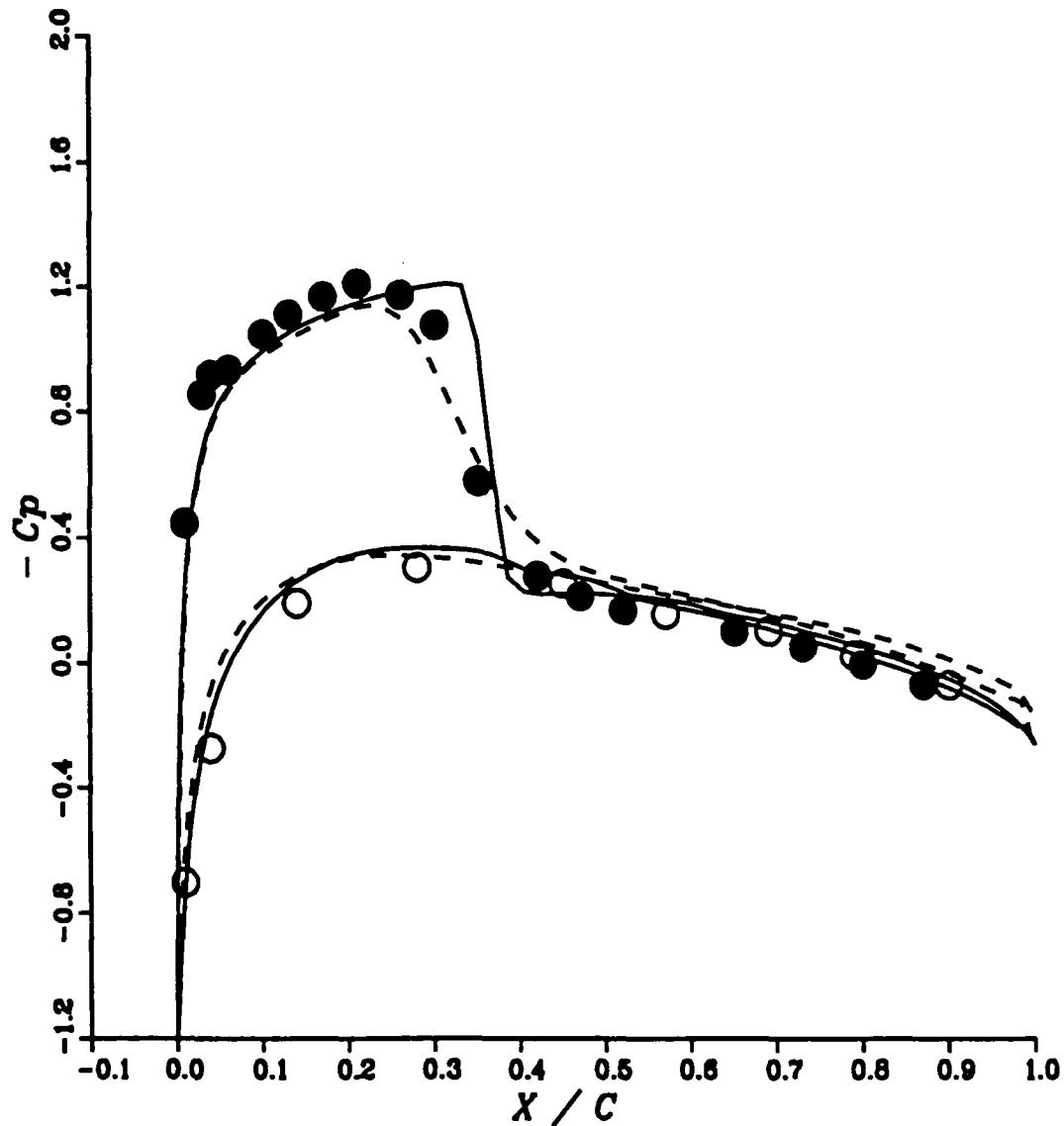
Fig. 22 Comparison of surface pressures for a lifting hovering rotor. $M_{tip} = 0.877$, $\alpha_t = 8°$, Re $= 3.83$x10^6 and $r_B = 0.89$.

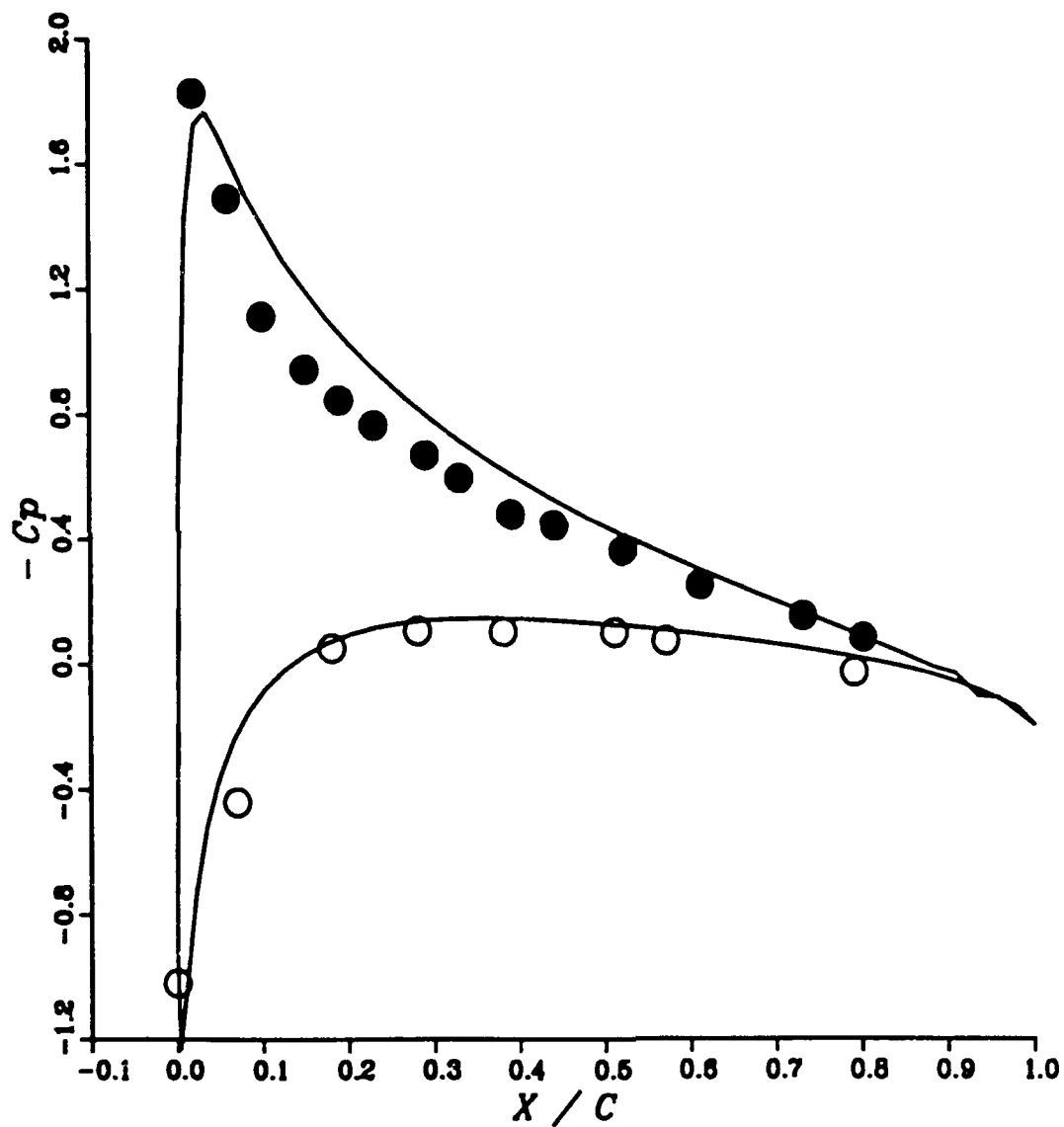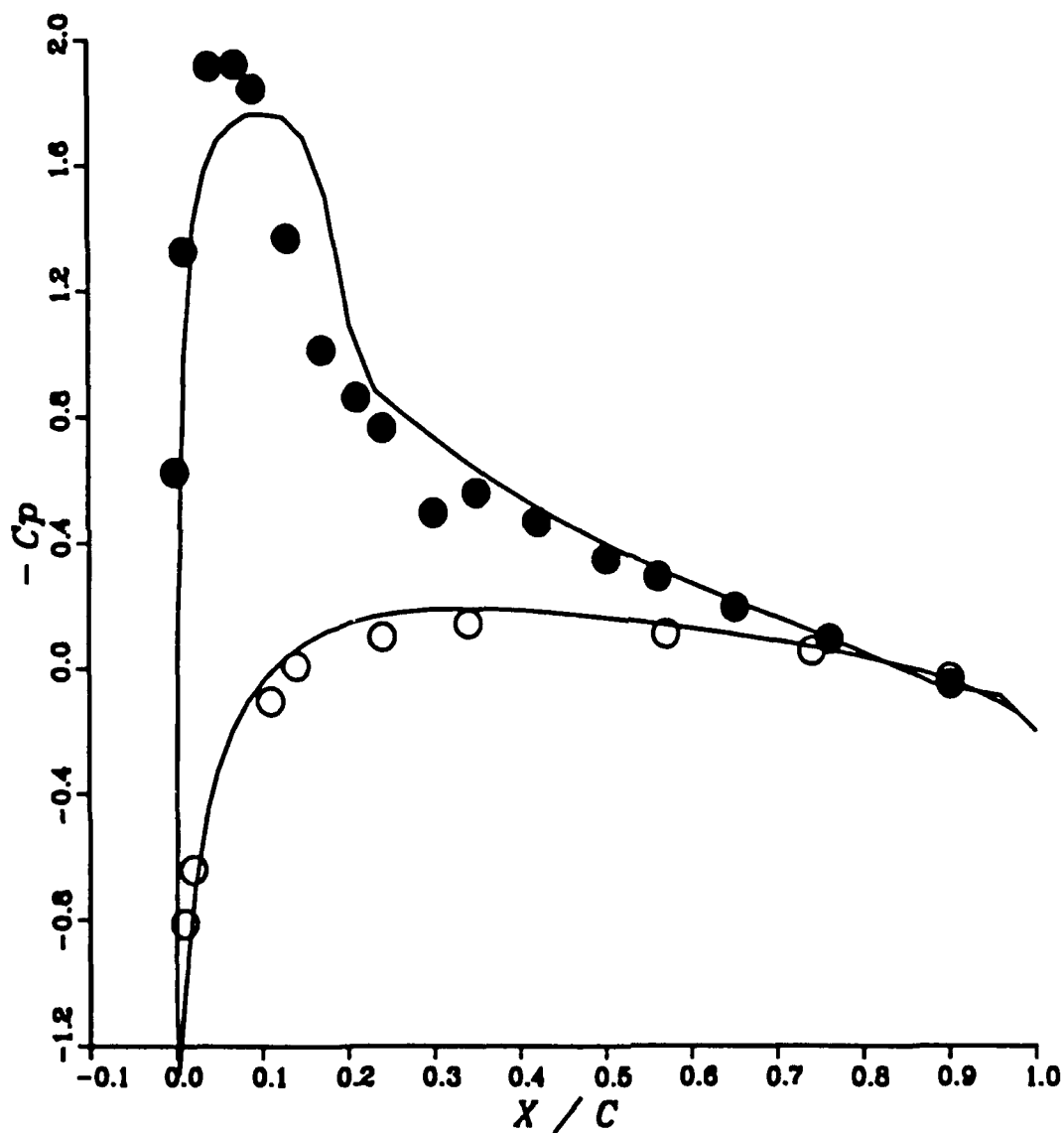|	M_{tip}	α_t	$2y/b$	
● ○	0.7940	12.000	0.5000	Experiment–Caradonna and Tung
——	0.7940	12.000	0.5298	Navier–Stokes Smallgrid Results
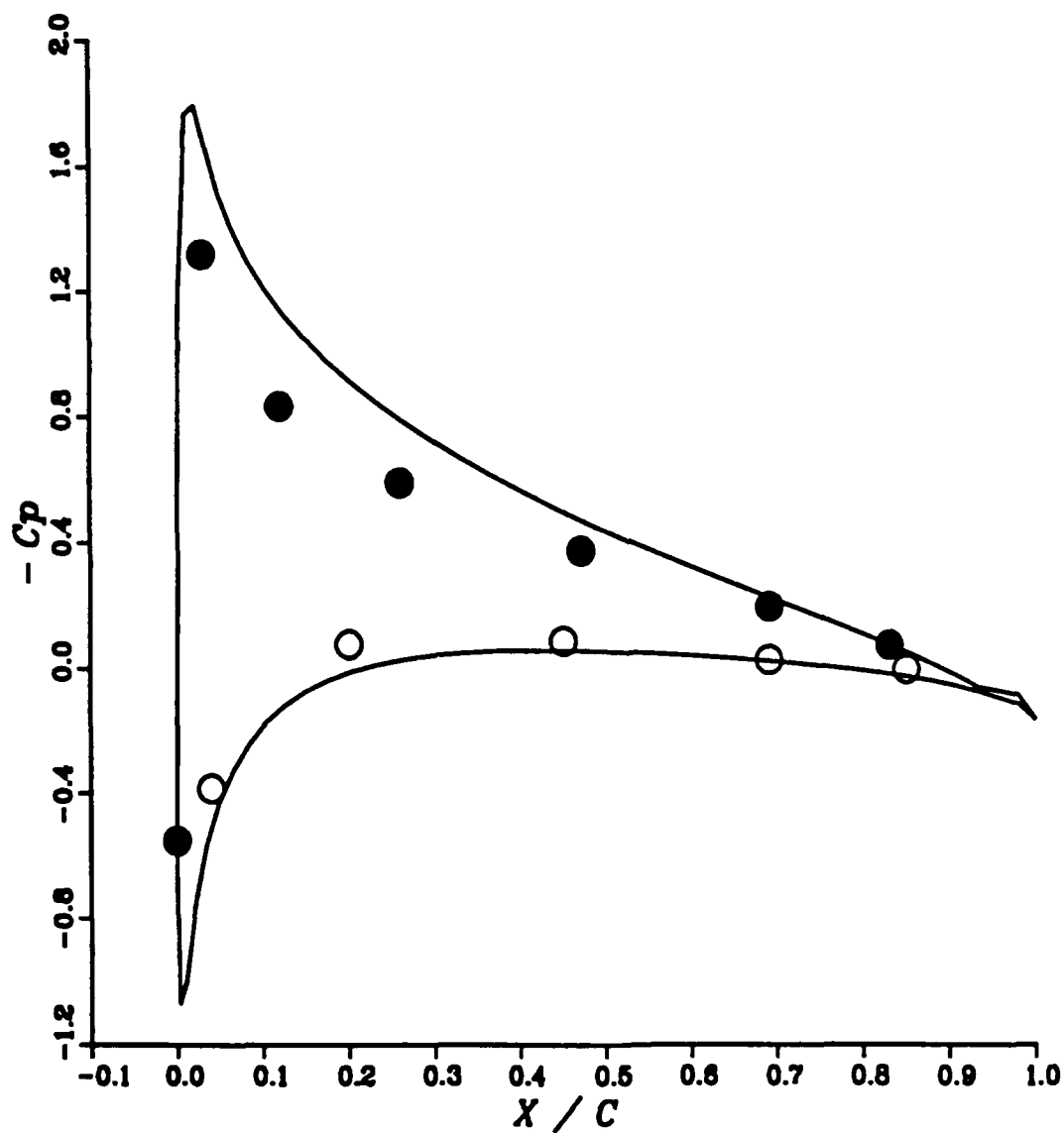
Fig. 23 Comparison of surface pressures for a lifting hovering rotor. $M_{tip} = 0.794$, $\alpha_t = 12°$, $Re = 3.53 \times 10^6$ and $r_B = 0.5$.

Fig. 24 Comparison of surface pressures for a lifting hovering rotor. $M_{tip} = 0.794$, $\alpha_t = 12°$, Re $= 3.53 \times 10^6$ and $r_B = 0.68$.

Fig. 25 Comparison of surface pressures for a lifting hovering rotor. $M_{tip} = 0.794$, $\alpha_t = 12°$, Re $= 3.53 \times 10^6$ and $r_B = 0.80$.
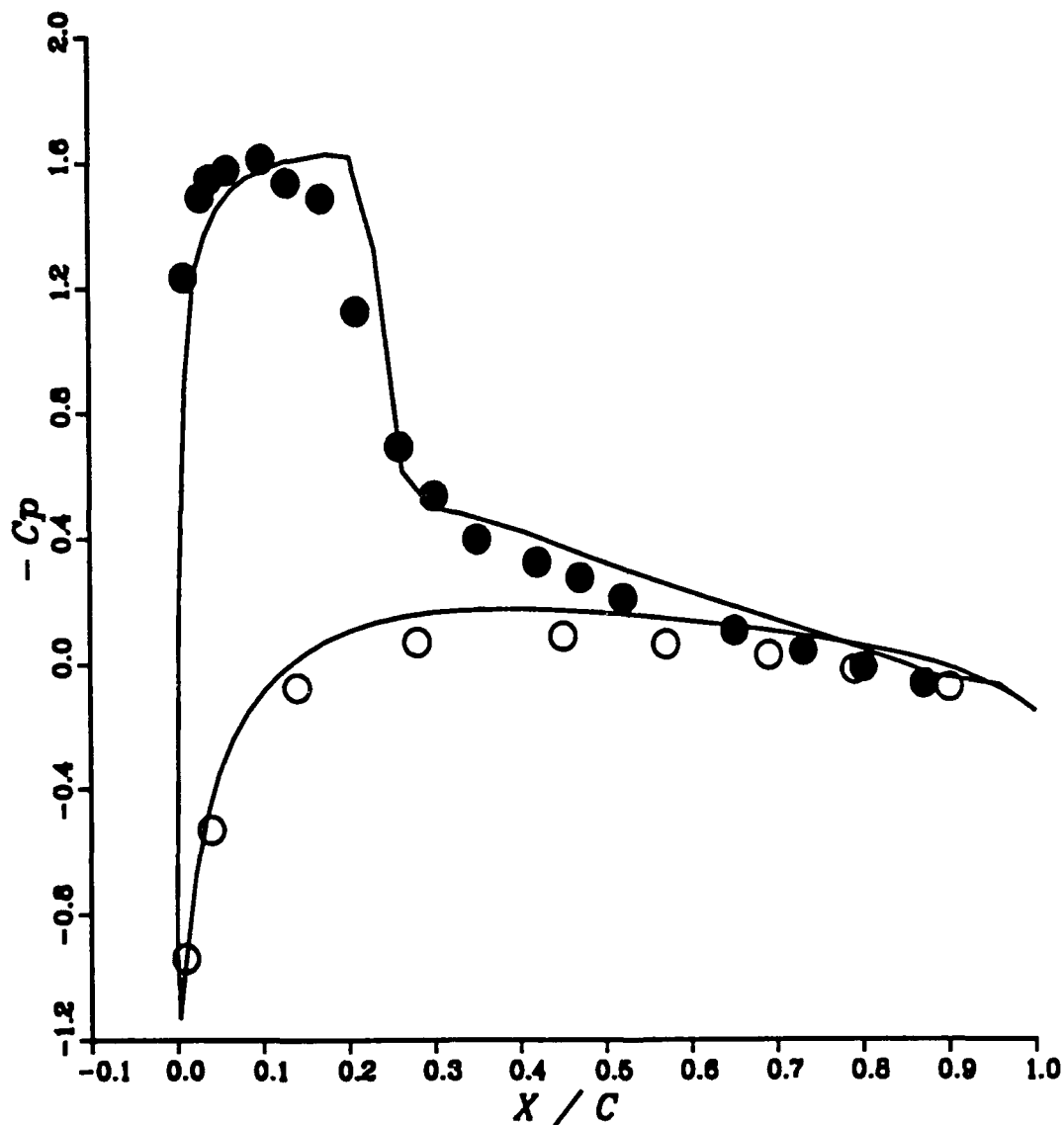
Fig. 26 Comparison of surface pressures for a lifting hovering rotor. $M_{tip} = 0.794$, $\alpha_t = 12°$, Re = 3.53×10^6 and $r_B = 0.89$.

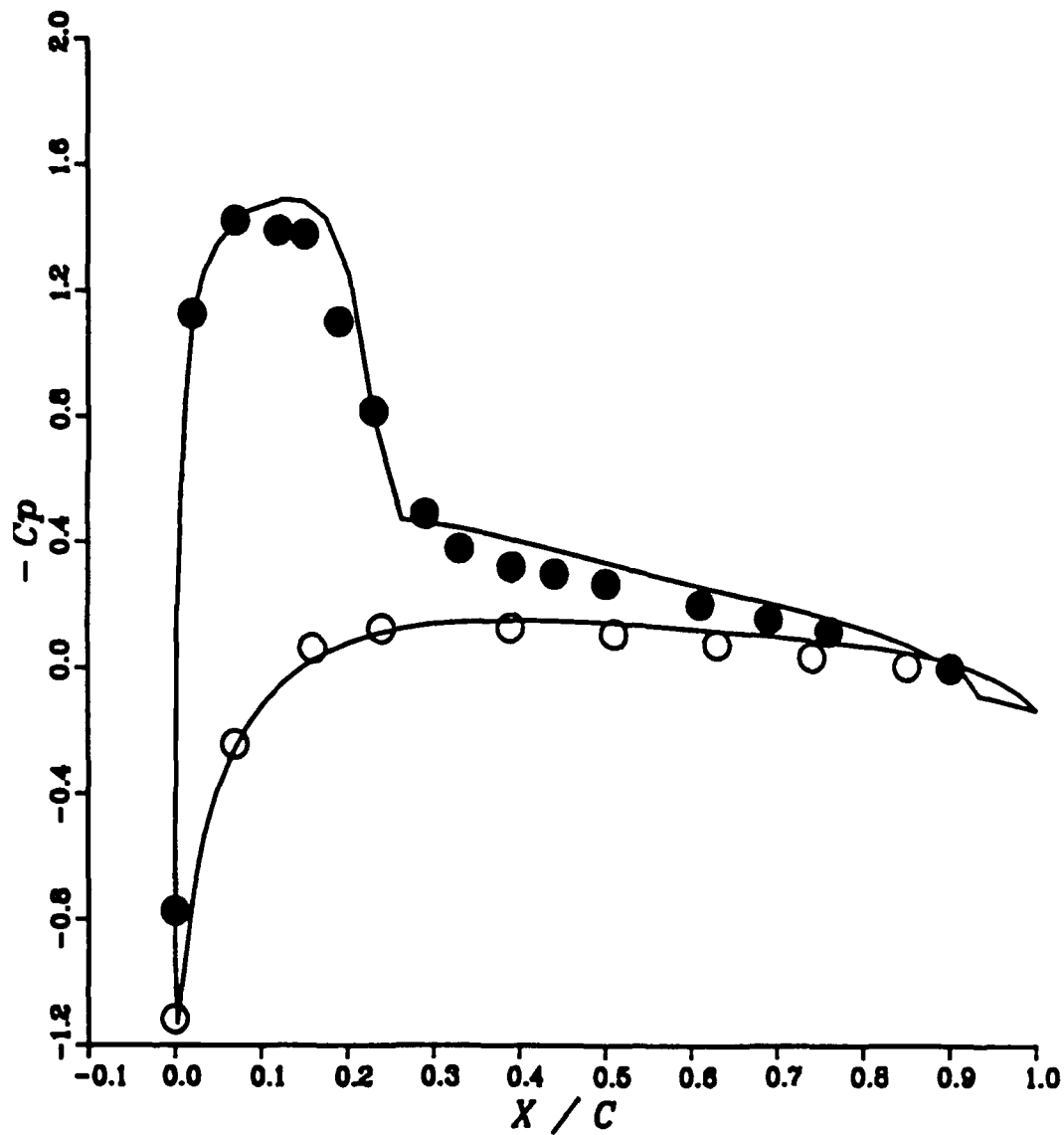|	M_{tip}	α_t	$2y/b$	
● ○	0.7940	12.000	0.9600	Experiment–Caradonna and Tung
——	0.7940	12.000	0.9578	Navier–Stokes Smallgrid Results

Fig. 27 Comparison of surface pressures for a lifting hovering rotor. $M_{tip} = 0.794$, $\alpha_t = 12°$, Re $= 3.53\text{x}10^6$ and $r_B = 0.96$.